Lorentz-force shifts in strong-field ionization with mid-infrared laser fields

Stephan Fritzsche [1,2,3,*] and Birger Böning [1,2]
[1] *Helmholtz-Institut Jena, D-07743 Jena, Germany*
[2] *GSI Helmholtzzentrum für Schwerionenforschung GmbH, D-64291 Darmstadt, Germany*
[3] *Theoretisch-Physikalisches Institut, Friedrich-Schiller-Universität Jena, D-07743 Jena, Germany*

(Received 22 March 2022; accepted 9 June 2022; published 12 July 2022)

In the past, the ionization of atoms and molecules by strong, mid-infrared (IR) laser fields has attracted recurrent interest. Measurements with different IR pulses have demonstrated the crucial role of the magnetic field on the electron dynamics, classically known as the Lorentz force $\mathbf{F}_L = q\,(\boldsymbol{\mathcal{E}} + \mathbf{v} \times \boldsymbol{\mathcal{B}})$, that acts upon all particles with charge q in motion. These measurements also require the advancement of theory beyond the presently applied methods. In particular, the strong-field approximation (SFA) is typically based on the dipole approximation alone and neglects both the magnetic field and the spatial dependence of the driving electric field. Here we show and discuss that several, if not most, observations from strong-field ionization experiments with mid-IR fields can be *quantitatively* explained within the framework of SFA, if the Lorentz force is taken into account by nondipole Volkov states in the formalism. The details of such a treatment are analyzed for the (peak) shifts of the polar-angle distribution of above-threshold ionization photoelectrons along the laser propagation, the steering of electron momenta by two not quite collinear laser beams, or the enhanced momentum transfer to photoelectrons in standing-light fields. Moreover, the same formalism promises to explain the generation of high harmonics and other strong-field rescattering phenomena when driven by mid-IR laser fields. All these results show how strong-field processes can be understood on equal footings within the SFA, if one goes beyond the commonly applied dipole approximation.

DOI: 10.1103/PhysRevResearch.4.033031

I. INTRODUCTION

If atoms are exposed to visible or near-infrared (IR) laser pulses with peak intensities larger than, say, 10^{13} W/cm^2, a number of nonlinear optical processes arise, such as above-threshold ionization (ATI), tunneling ionization, high-order-harmonic generation (HHG), or nonsequential double ionization (NSDI), to recall just a few of them [1,2]. In particular, the generation of high harmonics has been explored for more than two decades and has led to a number of important applications, including the production of attosecond pulses [3], high-energy harmonics within the water window [4], or even the imaging of the electron density of various atomic and molecular targets [5]. In addition, HHG with near- and mid-IR lasers bears the promise of the development of an ultrashort coherent light source in the extreme-ultraviolet and soft x-ray regions [6]. Indeed, such coherent radiation in the soft x-ray domain may help resolve the electron dynamics with attosecond temporal and sub-angstrom spatial resolution [7]. All these promises have recently initiated a number of strong-field ionization experiments at rather long wavelengths, $\lambda > 1200$ nm [8–10], and may pave the way to even longer ones [11].

However, all the nonlinear light-atom interaction processes from above rely on the interplay of weakly bound electrons with the laser field and, more often than not, on their laser-driven rescattering at the parent ions [12–14]. In mid-IR laser pulses, these electrons are thus affected by the Lorentz force [15], as shown schematically in Fig. 1, and which pushes the (oscillating) electrons away from their parent ions [16,17]. In a typical strong-field ionization measurement [cf. Fig. 1(a)] with just a single incident laser beam (red-wavy line) of intensity I, wavelength λ, and ellipticity ϵ, the laser-electron interaction leads to the emission of photoelectrons with asymptotic momentum $\mathbf{p}$ at the detector. In these measurements, the (magnetic) Lorentz force becomes visible in a nonzero momentum component p_z along the laser beam axis, often briefly referred to as *peak* shifts in the literature. When, as shown schematically in Fig. 1(b), the electron is released from its parent ion into the continuum, it is accelerated by the electric field $\boldsymbol{\mathcal{E}} = \boldsymbol{\mathcal{E}}(\mathbf{r}, t)$ up to the velocity $\mathbf{v}(t) = (v_x, v_y, 0)$. The classical Lorentz force $\mathbf{F}_L = q\,[\mathbf{v}(t) \times \boldsymbol{\mathcal{B}}(\mathbf{r}, t)]$ then contributes a shift $\Delta\, p_z$ to the (longitudinal) momentum along the beam propagation, which becomes measurable for sufficiently high velocities of the electron. Figure 1(c) displays the path of the photoelectron within the *reaction* plane as spanned by the polarization (x axis) and propagation (z axis) directions of the laser. Within each optical cycle, a quasifree electron propagates a distance r_z along the beam axis, and with paths shown for two characteristic wavelengths $\lambda = 800$ nm (blue-dashed line) and $\lambda = 1600$ nm (black-solid line) of the incident beam. This quasifree motion also leads to the frequently discussed *figure-eight motion* of the electron in the field with amplitude $\beta_0 = \frac{\mathcal{E}_0^2}{16c\omega^3} \sim I\lambda^3 \sim U_p\lambda \gtrsim a_o$ along the beam axis for

* s.fritzsche@gsi.de

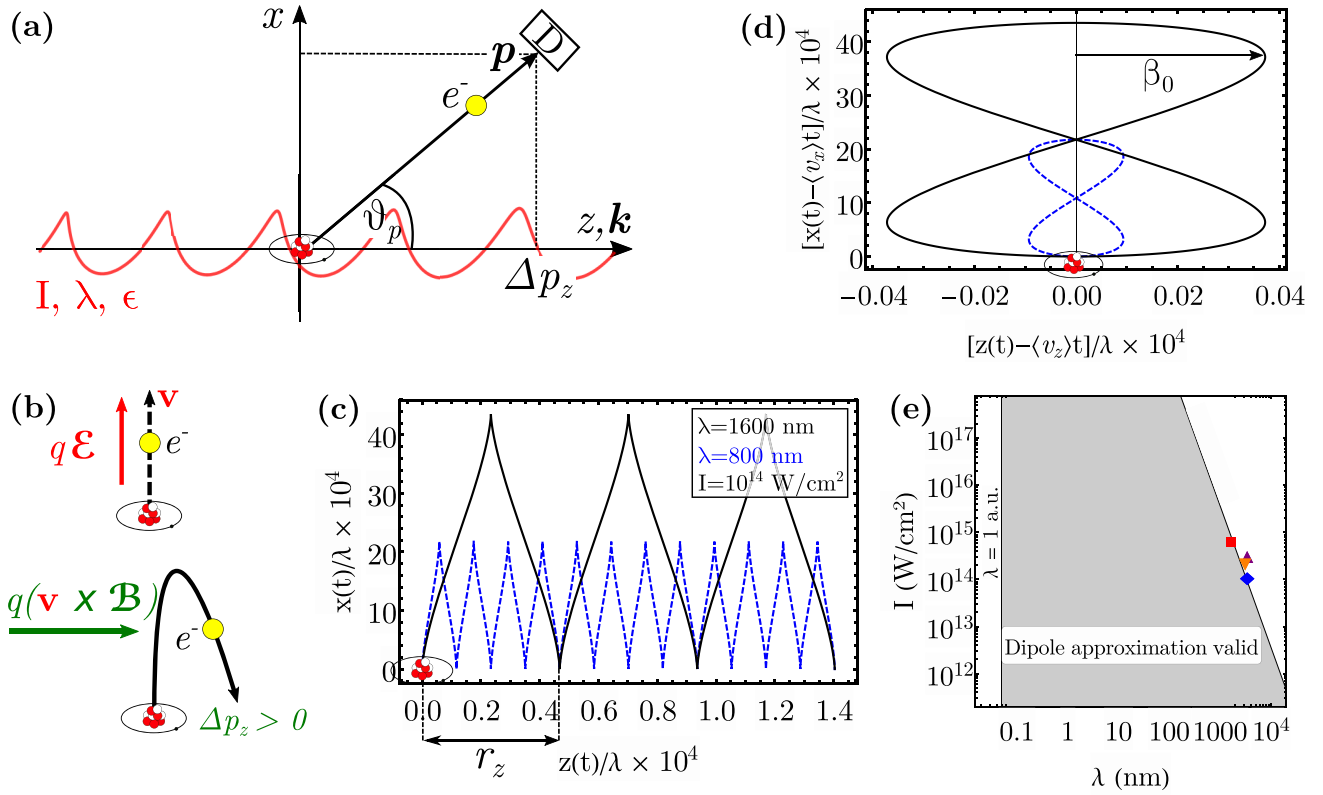

FIG. 1. Influence of the Lorentz force upon strong-field ionization processes. (a) Typical setup of a strong-field ionization measurement with a single incident laser beam (red) of intensity I, wavelength λ, and ellipticity ϵ. The interaction of the laser field with the atomic target leads to photoelectrons with asymptotic momentum $\mathbf{p}$ at the detector. In these measurements, the (magnetic) Lorentz force becomes visible first of all in a nonzero momentum component p_z along the laser beam axis. (b) When the electron is released from its parent ion into the continuum, it is accelerated within the (transverse) polarization plane by the electric field $\boldsymbol{\mathcal{E}} = \boldsymbol{\mathcal{E}}(\mathbf{r}, t)$ up to the velocity $\mathbf{v}(t) = (v_x, v_y, 0)$. The classical Lorentz force $\mathbf{F}_L = q[\mathbf{v}(t) \times \boldsymbol{\mathcal{B}}(\mathbf{r}, t)]$ then contributes a shift Δp_z to the (longitudinal) momentum along the beam propagation, which becomes measurable for sufficiently high velocities of the electron. (c) Path of the photoelectron within the *reaction* plane, where the electron propagates a distance r_z along the beam axis within each optical cycle. Paths are shown for two characteristic wavelengths $\lambda = 800$ nm (blue-dashed line) and $\lambda = 1600$ nm (black-solid line) of the incident beam. (d) Characteristic *figure-eight motion* of the electron in the field with amplitude β_0 along the beam axis, if the constant averaged drift $\langle v_z \rangle t$ is subtracted. For sufficiently large amplitudes $\beta_o \gtrsim a_o$, the Lorentz force is therefore no longer negligible and requires a proper quantum treatment. (e) Wavelength-intensity domain (gray) in which the dipole approximation is considered to be valid for a single driving laser beam [18]. Colored symbols are shown for typical wavelengths and intensities as applied in recent strong-field ionization experiments: blue diamond [19], purple triangle [20], and orange triangle [21]. Moreover, the black circle displays the typical laser parameters for near-IR experiments with $\lambda = 800$ nm. See text for further discussion.

sufficiently long wavelength [Fig. 1(d)], if the averaged drift $\langle v_z \rangle t$ is subtracted. Here, moreover, U_p denotes the ponderomotive energy of the photoelectron, i.e., its (classical) cycle-averaged kinetic energy in the continuum, and I_p the ionization potential of the target atom, which are often summarized in terms of the Keldysh parameter $\gamma = \sqrt{I_p/2\,U_p} \propto \sqrt{I_p/\beta_0} < 1$ [22]. For sufficiently large $\beta_o \geqslant a_o$, therefore, the Lorentz force is no longer negligible and requires a proper quantum treatment. This is readily seen also from the (gray) wavelength-intensity domain in Fig. 1(e), for which the dipole approximation is considered to be valid for a single driving laser beam. This domain is limited for small wavelength to the left by the size of the target atoms and for long wavelength to the right by the Lorentz drift along the beam axis. Colored symbols are shown in this figure for typical wavelengths and intensities as applied in recent strong-field ionization experiments. In addition, the black circle displays the typical laser parameters for near-IR experiments with $\lambda = 800$ nm.

Obviously, the large amplitude β_o of the oscillating electron makes it necessary to go beyond the standard *dipole* approximation, i.e., beyond a homogeneous electric and merely time-dependent field. For plane-wave laser beams, various *nondipole* methods have therefore been developed during recent years, including the (single-beam) nondipole strong-field approximation (SFA) by Titi *et al.* [23], the quasirelativistic SFA by Krajewska *et al.* [24], as well as the nondipole Volkov solutions to the Schrödinger equation by He and co-workers [25]. All these methods explain the considered experiments with mid-IR laser pulses reasonably well, while Ref. [24] in particular showed how the retardation and recoil corrections already contribute to the peak shifts $\propto 1/c$ in the quasirelativistic SFA. These approaches indeed account for major parts of the Lorentz force for computing the peak shifts of the photoelectrons along the beam propagation and, by including rescattering terms into the SFA, they have been restricted to copropagating plane-wave beams. Until the present,

TABLE I. Useful parameters that help characterize the (valence-shell) electronic motion of target atoms with ionization potential I_p in strong laser fields. For an incident pulse with either purely linear ($\epsilon = 0$) or circular polarization ($\epsilon = \pm 1$), wavelength λ (nm), and peak intensity I (W/cm^2), the laser-electron interaction can be examined in terms of the ponderomotive potential U_p (eV) to designate the mean classical energy of a quasi-free electron in the field, the Keldysh parameter γ to relate the strengths of the electrostatic atomic and the laser (electric) fields, as well as the mean Lorentz force $\langle F_{L,z}\rangle$ that acts upon a (classical) electron with binding energy $\varepsilon = -I_p$. Moreover, the Lorentz force pushes the electron per laser cycle by a distance r_z along the propagation direction of the laser beam. After the first return of the electron to the parent ion, its binding energy at the closest approach is therefore lowered by the factor $R_b = \epsilon_b(r_z)/I_p$, which nicely indicates its delocalization from the ionic core. Below, all parameters are shown for krypton ($I_p = 14$ eV), which has been frequently applied in strong-field experiments.

λ (nm)	I (W/cm^2)	U_p (eV)	γ	$\langle F_{L,z}\rangle$ (10^{-4} a.u.)	r_z (pm)	R_b
			Linearly polarized laser beam ($\epsilon = 0$)			
800	10^{13}	0.6	3.4	0.2	2.8	0.95
	5×10^{13}	3.0	1.5	1.1	14.0	0.78
	10^{14}	6.0	1.1	2.3	28.1	0.65
1600	10^{13}	2.4	1.7	0.5	22.5	0.70
	5×10^{13}	12.0	0.8	2.3	112	0.31
	10^{14}	23.9	0.5	4.6	225	0.19
3200	10^{13}	9.6	0.9	0.9	180	0.23
	5×10^{13}	47.8	0.4	4.6	899	0.05
	10^{14}	95.6	0.3	9.3	1799	0.03
			Circularly polarized laser beam ($\epsilon = 1$)			
1600	10^{13}	2.4	1.7	0.2	15.0	0.78
	5×10^{13}	12.0	0.8	1.1	74.8	0.41
	10^{14}	23.9	0.5	2.3	150	0.25

only the nondipole SFA from Ref. [26], derived by us, is able to support both the discrete and continuous superpositions of plane-wave beams and, hence, a rather general *spatial* dependence of the laser field for the motion of the electrons in the continuum. This nondipole SFA for spatially structured beams also provides a nonzero and observable peak shift Δp_z (of the maxima) in the photoelectron momentum distributions of the ATI spectra in good-to-excellent agreement with experiment.

To better understand the role of the Lorentz force upon strong-field ionization and rescattering processes, we theoretically analyze selected *scenarios* that have been experimentally realized or discussed in good detail in the literature [19,21]. Emphasis is placed on the nondipole SFA from Ref. [26] and how this approximation can be utilized to quantitatively predict the energy and momentum shifts in the observed spectra. In Sec. II, we shall recall the theoretical background of the nondipole SFA by first elucidating the role of the Lorentz force in terms of a few *characteristic* parameters. We also discuss both the construction of the Volkov states for spatially structured fields as well as the direct SFA amplitude, before we shall make the influence of the combined—electric *and* magnetic—fields upon the electron dynamics explicit. In Sec. III, we then apply this theory to a number of atomic strong-field phenomena, including the peak shifts in the polar-angle distribution (PAD) of the ATI photoelectron along the laser propagation, the steering of the electron momenta by noncollinear laser beams, or the enhanced momentum transfer to photoelectrons in standing-light fields. This section demonstrates how quite different observations can be explained, both qualitatively *and* quantitatively, if the Lorentz force is accounted for in a quantum description of strong-field atomic processes. This includes the promise to explain the generation of high harmonics as well as other strong-field rescattering phenomena when driven by mid-IR laser fields. Finally, a short summary and outlook are given in Sec. IV.

II. THEORETICAL BACKGROUND

A. Parameters for characterizing the motion of atomic electrons in mid-IR laser fields

In strong laser fields, a weakly bound atomic electron follows the laser field quite analogous to a *free* electron, initially at rest, though with various constraints due to its parent ion. Several parameters can be readily derived to characterize the motion of such quasifree electrons for target atoms with ionization potential I_p. Apart from the ponderomotive potential U_p and the Keldysh parameter $\gamma = \sqrt{I_p / 2\,U_p}$, which emphasize the (mean) kinetic energy as well as (its ratio to) the ionization potential, the magnetic field of the incident beam pushes the electron away from its parent ion along the beam axis. This influence of the magnetic field can qualitatively be understood in terms of the Lorentz force, which acts upon a classical electron with potential energy $-I_p$ and leads to a drift r_z per laser cycle; cf. the discussion of Fig. 1. This drift, of course, also lowers the effective binding energy by a factor $R_b = \varepsilon_b(r_z)/I_p = -Z^{\,(\mathrm{eff})}/I_p\,r_z$ at its first return to the ion and eventually becomes visible in all strong-field ionizations as well as rescattering processes. Table I displays these characteristic parameters for a krypton gas target as frequently applied in many measurements. These parameters are displayed for the three wavelengths $\lambda = 800$, 1600, and 3200 nm as well as the peak intensities $I = 10^{13}$, 5×10^{13}, and 10^{14} W/cm^2, respectively. For linearly polarized light, in particular, the mean Lorentz force $\langle F_{L,z}\rangle$, which needs to be integrated numerically, and the drift per laser cycle r_z rapidly increase with the wavelength λ and intensity I of the laser beam. While the Lorentz force is linear in both the wavelength

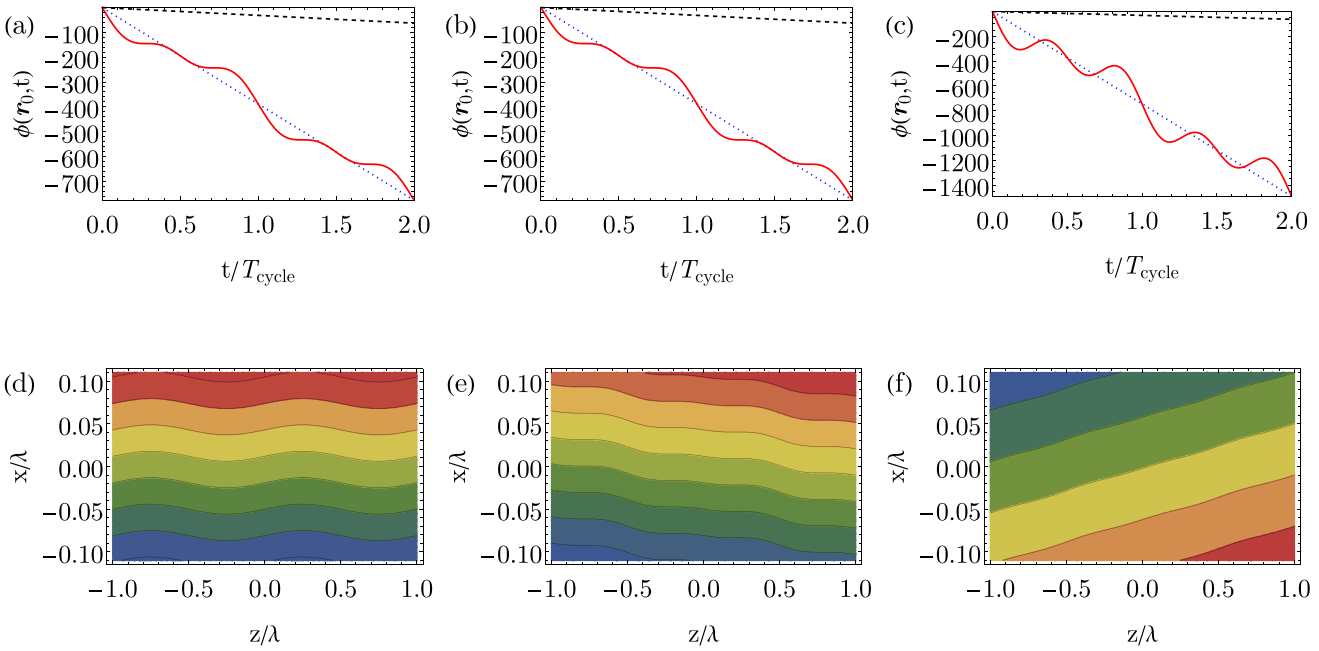

FIG. 2. Total phase $\phi(\mathbf{r},t)$ of the (free-)electron Volkov states as a function of time, shown for different laser fields. Results are displayed for a single plane-wave beam and two noncollinear beams by applying three different approximations: The single-beam dipole-Volkov phase (left column) is compared with the (single-beam) nondipole phase (middle column) as well as the nondipole phase for two not quite collinear beams (right column), respectively. (a)–(c) The time dependence of the total phase $\phi(\mathbf{r}_o,t)$ at the origin $\mathbf{r}_o=0$. The red-solid lines display the full phase $\phi(\mathbf{r}_o,t)$ for the three different Volkov solutions from above, including (a) $\phi(\mathbf{r}_o,t)=\mathbf{p}\,\mathbf{r}-S_V(t)$ and (b),(c) $\phi(\mathbf{r}_o,t)=\mathbf{p}\,\mathbf{r}-\Gamma(\mathbf{r}_o,t)$. These total phases are also compared to the purely ponderomotive phase $\phi^{\,(\text{ponderomotive})}(\mathbf{r}_o,t)=\mathbf{p}\,\mathbf{r}-U_p\,t$ (blue-dotted lines) as well as the phase of a free electron $\phi^{\,(\text{free})}(\mathbf{r}_o,t)=\mathbf{p}\,\mathbf{r}-p^2/2\,t$ (black-dashed lines). (d)–(f) A contour plot of the total phase $\phi(\mathbf{r},t_o)$ of the Volkov solutions at constant time $t_o=T_{\rm cycle}/2$ *within* the $x-z$ reaction plane. While the electron wave mainly moves along the polarization (x) axis, the total phase also depends on the beam propagation (z axis), but—like a corrugated cardboard—is independent of y. The colors in the bottom row are drawn only to guide the eyes and the following parameters are employed: $I=10^{15}$ W/cm^2, $\lambda=1600$ nm, linear polarization ($\epsilon=0$) along the x axis, $\mathbf{p}=(\sqrt{2E_p},0,0)$, and $E_p=5\,\omega$, respectively. In the right column, a second identical beam propagates under the angle $\delta=+5^\circ$ with respect to the first one *within* the $x-z$ plane. See text for further discussion.

and intensity, the distance r_z increases even quadratically with the wavelength. At $\lambda=3200$ nm, for instance, the electron is easily pushed more than 10 a.u. ≈500 pm within a single laser cycle away from the parent ion. As seen from the relative binding energy R_b in the last column, the electron is only very weakly bound at its first return and can therefore hardly be recaptured by its ion. For circularly polarized light, the Lorentz force is smaller and, hence, the electron will remain stronger bound to its parent ion since $\mathcal{E}_o\propto\sqrt{I/(1+\epsilon^2)}$.

While the parameters from Table I clearly affirm the role of the Lorentz force in strong-field processes with mid-IR laser fields, a more advanced quantum description is required in order to predict the observed spectra and shifts also *quantitatively*. Below, we shall make use of the nondipole SFA for analyzing how the Lorentz force contributes to the ATI, the deflection of electrons in a standing-light field (Kapitza-Dirac effect), or even the generation of high harmonics with mid-IR fields. To provide a consistent theoretical framework, we first recall how the nondipole SFA can be applied to account for the spatial structure and, hence, the magnetic field of the incident laser pulses. In particular, here we examine how the nondipole contributions from the Volkov solutions enter the strong-field amplitude and naturally give rise to terms that can be discussed individually for all the processes mentioned above. While we restrict ourselves to just the relevant stepping stones in this discussion, we refer the reader to the literature for all further mathematical details [26]. Atomic units ($m_e=\hbar=e^2/4\pi\epsilon_o=1$) are used throughout this paper, unless stated otherwise.

B. Electrons in strong laser fields. Volkov states

In an external electromagnetic field with vector potential $\mathbf{A}(\mathbf{r},t)$, an electron follows, most generally and within velocity gauge, the time-dependent Schrödinger equation,

$$i\frac{\partial}{\partial t}\chi(\mathbf{r},t)=\frac{1}{2}[\mathbf{p}+e\mathbf{A}(\mathbf{r},t)]^2\chi(\mathbf{r},t), \tag{1}$$

where $\mathbf{p}$ denotes the kinetic momentum and $[\mathbf{p}+e\mathbf{A}(\mathbf{r},t)]$ the so-called (conjugate) canonical momentum of the electron *within* the field. While this equation cannot be solved so readily for a spatially dependent vector potential, the well-known plane-wave solutions for $\mathbf{A}(\mathbf{r},t)\equiv 0$ are simply given by

$$\chi_{\mathbf{p}}(\mathbf{r},t)\equiv\frac{1}{(2\pi)^{3/2}}\,e^{i\,\phi(\mathbf{r},t)}\;=\;\frac{1}{(2\pi)^{3/2}}\,e^{i\,(\mathbf{p}\cdot\mathbf{r}-\frac{p^2}{2}t)}.$$

These solutions describe electrons with well-defined momentum $\mathbf{p}$, whose wave fronts move with phase velocity $\mathbf{v}=-\frac{1}{m}\frac{\partial\phi}{\partial t}=p/m$ and, thus, immediately reflect the nonrelativistic energy-momentum relation of all free particles, as also shown by the black-dashed curve in Fig. 2(a).

Solutions for the time-dependent Schrödinger equation (1) are also known for monochromatic and purely time-dependent light fields $\mathbf{A}(t) \neq \mathbf{A}(\mathbf{r}, t)$, i.e., in dipole approximation,

$$\chi_{\mathbf{p}}(\mathbf{r}, t) = \frac{1}{(2\pi)^{3/2}}\, e^{i\mathbf{p}\cdot\mathbf{r}}\, e^{-iS_V(t)},$$
$$S_V(t) = \frac{1}{2}\int^t d\tau\ [\mathbf{p} + \mathbf{A}(\tau)]^2. \tag{2}$$

These solutions still describe electrons with well-defined kinetic momentum $\mathbf{p}$ and are referred to as Volkov states in the literature [27]. They are often utilized in the treatment of strong-field ionization processes for analyzing the asymptotic momentum $\mathbf{p} = (p, \vartheta, \varphi)$ of photoelectrons at the detector, once the electrons have entered the field-free region. With these solutions, the Volkov phase $S_V(t)$ gives rise to a discrete energy spectrum that readily describes the ATI peaks [28–30]. Mathematically, these solutions already contain the frequencies that occur in a Fourier expansion of the vector potential, i.e., the fundamental frequency and all the overtones of the driving beam. In contrast to the *nondipole* Volkov states below, however, the laser field here only influences the energy of the photoelectrons, while their momentum remains restricted to the $(x - y)$ polarization plane.

The use of the Volkov solutions (2) in the computation of transition and ionization amplitudes is therefore in line with the *dipole* approximation, in which just a homogeneous electric field $\boldsymbol{\mathcal{E}}(t)$ is assumed for the entire motion of the electron within the laser field. Below, we shall refer to these solutions as *dipole-Volkov* states in order to clearly distinguish them from a more generalized formulation of the laser-electron interaction. The red line in Fig. 2(a) displays as a function of time t the contribution of the oscillating laser field to the total phase,

$$\phi(\mathbf{r}_o, t) = \mathbf{p}\cdot\mathbf{r}_o - S_V(t)$$
$$= \mathbf{p}\cdot\mathbf{r}_o - (p^2/2 + U_p)t + p_x A_0\ \sin(\omega t),$$

of the photoelectron. While the kinetic momentum and the ponderomotive energy U_p alone (blue-dotted line) lead to a linear decrease of the phase, the vector potential in the Volkov phase gives rise to oscillations around this straight line. For a fixed time t_o, moreover, the lines of constant phase exhibit a sinusoidal dependence in the $x - z$ reaction plane [cf. Fig. 2(d)], instead of just straight lines as we expect for free electrons.

Unfortunately, any spatial dependence of the vector potential $\mathbf{A}(\mathbf{r}, t)$ prevents the straightforward solution of the time-dependent Schrödinger equation (1). However, an approximate Volkov-like solution can still be constructed for most laser fields that can be expressed as a superposition of spatial modes, either in discrete or integral form. For a finite number of *discrete* laser modes, especially, these solutions were first derived by Rosenberg and Zhou [31], including modes with nonparallel wave vectors $\mathbf{k}$, and were recently generalized by us [26] in order to account for *continuous* superpositions of laser modes as well. In principle, this generalization enables us to incorporate any spatial dependence of the driving beam, e.g., Gaussian or twisted light beams, into the (quantum) dynamics of the photoelectron [32], though often at the price of quite sophisticated integrals. These generalized *nondipole* Volkov solutions can be written by means of a modified Volkov phase $\Gamma(\mathbf{r}, t)$ as [26]

$$\chi_{\mathbf{p}}(\mathbf{r}, t) = \frac{1}{(2\pi)^{3/2}}\, e^{i(\mathbf{p}\cdot\mathbf{r} - \frac{p^2}{2}t)}\, e^{-i\,\Gamma(\mathbf{r},t)}, \tag{3}$$
$$\Gamma(\mathbf{r}, t) = \Gamma_1(\mathbf{r}, t) + \Gamma_2(\mathbf{r}, t) + \Gamma_3(\mathbf{r}, t) + \mathcal{O}\left(\frac{\beta_0^{3/2}}{a_0\lambda^{1/2}}\right), \tag{4}$$

which consists of three contributions $\Gamma_i(\boldsymbol{r}, t)$, $i = 1, 2, 3$, due to the interaction of the free electron with different parts of the vector potential. The complete expression of the modified Volkov phase (4) is shown below in Sec. 1 of the Appendix. The first term $\Gamma_1(\boldsymbol{r}, t) \propto \frac{p e A_o}{m_e c\omega}$ scales with the product of the kinetic momentum p and the field-induced momentum eA_o of the ejected electron, while the second term $\Gamma_2(\boldsymbol{r}, t) \propto U_p/\omega$ is just proportional to the ponderomotive energy, normalized to the frequency ω of the laser beam. Finally, the third term $\Gamma_3(\boldsymbol{r}, t) \propto \frac{eA_o}{m_e c} \cdot \frac{U_p}{\omega}$ depends on the product of the field-induced momentum and the frequency-normalized ponderomotive potential. All further terms are of higher order in the amplitude A_o of the vector potential and are captured by the symbol $\mathcal{O}$. These additional terms can be safely neglected as long as the magnitude β_0 of the classical figure-eight motion is small or comparable with regard to the Bohr radius a_0. This is also seen directly from the argument $x = \frac{\beta_0^{3/2}}{a_0\sqrt{\lambda}}$ of $\mathcal{O}(\ldots)$ which becomes small ($x \ll 1$) for $\beta_o \simeq a_o$, whereas a relativistic treatment is required and has been suggested right from the beginning for $x \gtrsim 1$ [24,26].

The modified phase (4) also contributes, of course, to the total phase $\phi(\mathbf{r}, t)$ in Figs. 2(b) and 2(c). In the lower row of this figure, a contour plot is shown of the total phase $\phi(\mathbf{r}, t_o)$ at some constant time $t_o = T_{\text{cycle}}/2$ of the Volkov solutions *within* the $x - z$ reaction plane. While the electron mainly moves along the polarization axis (x axis), the total phase also depends on the beam propagation (z axis), but—like a corrugated cardboard— is independent of y. To make the different contributions visible, these phases are displayed for the (exaggerated) intensity $I = 10^{15}$ W/cm^2, wavelength $\lambda = 1600$ nm, as well as for a linearly polarized ($\epsilon = 0$) beam along the x axis that leads to photoelectrons with $\mathbf{p} = (\sqrt{2E_p}, 0, 0)$ and $E_p = 5\,\omega$, respectively. In the right column, moreover, a second identical beam has been assumed to propagate under the angle $\delta = +5^o$ with respect to the first one *within* the reaction plane.

The solutions (3) and (4) are exact up to the order (v/c) in the velocity of the electrons and simplify to the known (dipole) Volkov states (2) for a single plane-wave laser field, if the wave vector $\boldsymbol{k} \to 0$ and for nonrelativistic electrons. Since these solutions are valid for any superposition of plane-wave modes, they are no longer restricted to monochromatic, and thus time-harmonic, beams, but can (in principle) also be evaluated for few-cycle laser pulses.

It is instructive to make the generalized nondipole Volkov states (3) and (4) explicit for various spatially structured field configurations. For a single elliptically polarized beam with ellipticity $-1 \leqslant \epsilon \leqslant 1$ and wave vector $\mathbf{k}_o = \omega_o/z\mathbf{e}_z$, which propagates along the z axis, for example, the vector potential

can be written as [13]

$$\mathbf{A}(\mathbf{r},t) = \frac{A_0}{\sqrt{1+\epsilon^2}}[\cos(\mathbf{k}_0\cdot\mathbf{r}-\omega_0 t)\,\mathbf{e}_x - \epsilon\,\sin(\mathbf{k}_0\cdot\mathbf{r}+\omega_0 t)\,\mathbf{e}_y]. \quad (5)$$

For such a beam, the modified Volkov phase (4) takes the form

$$\Gamma(\boldsymbol{r},t) = \rho_\epsilon\,\sin\left(u_{\boldsymbol{k}_0}+\varphi_p^{(\epsilon)}\right) + \alpha\frac{\epsilon^2-1}{\epsilon^2+1}\,\sin\left(2\,u_{\boldsymbol{k}_0}\right) - 2\,\alpha u_{\boldsymbol{k}_0},$$
$$\rho_\epsilon = -\frac{A_0}{\omega\sqrt{1+\epsilon^2}}\,\frac{p^{(\epsilon)}}{1-\boldsymbol{p}\cdot\boldsymbol{k}_0/\omega}, \quad (6)$$
$$\alpha = \frac{\tilde{U}_p}{2\omega} = \frac{U_p}{2\omega\,(1-\mathbf{p}\cdot\mathbf{k}_0/\omega)},$$

where ρ_ϵ refers to a product of the kinetic and field-induced photoelectron momenta, while α denotes the modified ponderomotive energy $\tilde{U}_p = \frac{U_p}{1-\boldsymbol{p}\cdot\boldsymbol{k}_0/\omega}$, divided by $2\,\omega$. Moreover, $u_{\mathbf{k}_0} = \mathbf{k}_0\cdot\mathbf{r}-\omega_0 t$ is the phase of the vector potential and $p^{(\epsilon)}, \varphi_p^{(\epsilon)}$ just describe the modulus and azimuthal angle of an auxiliary and polarization-dependent momentum vector $\mathbf{p}^{(\epsilon)} = (p_x,\,\epsilon p_y,\,0) = (p^{(\epsilon)},\,\pi/2,\,\varphi_p^{(\epsilon)})$ in Cartesian and, respectively, spherical representation, and that lies within the polarization plane. While, at the first glance, this notation looks slightly overloaded, it has been found to be helpful to express the modified Volkov phase (4) for other field configurations, as shown below. In comparison with the general expression (4), the first term on the right-hand side of (6) arises from $\Gamma_1(\boldsymbol{r},t)$, and the second and third terms arise from $\Gamma_2(\boldsymbol{r},t)$, while the contribution from $\Gamma_3(\boldsymbol{r},t)$ simply vanishes for a single plane-wave beam; cf. Sec. 1 of the Appendix. The terms in (6) for a single elliptically polarized beam will become important for our discussions of the peak shifts in the PAD of the photoelectrons below. The solutions (6) still account for both the electric and magnetic fields of the laser beam upon the motion of the electron and, hence, enable us to include the Lorentz force in the quantum description. When compared to the dipole approximation above, we only need to replace the time-harmonic dependence $-\omega\,t$ by the full phase of the vector potential $\mathbf{k}_0\cdot\mathbf{r}-\omega_0\,t$ in the $\sin(\ldots)$ functions. This also shows how the Lorentz force enters the Volkov phase $\Gamma(\boldsymbol{r},t)$ by the absorption of discrete photon momenta $\hbar\,\mathbf{k}_0$ and will be made more explicit in the discussion of peak shifts below. In the dipole limit $\mathbf{k}_0\to 0$, again, only the time-dependent terms will remain in the Volkov phase and then just refer to a change of the *energy* of the photoelectrons.

Another field configuration of great practical interest refers to the superposition of two noncollinear beams, for which the combined electric and magnetic fields are given by the sum of the individual vector potentials,

$$\mathbf{A}(\mathbf{r},t) = \mathbf{A}_1(\mathbf{r},t) + \mathbf{A}_2(\mathbf{r},t), \quad (7)$$

$$\mathbf{A}_j(\mathbf{r},t) = A_j^{(0)}[\cos(\mathbf{k}_j\cdot\mathbf{r}-\omega_j t)\mathbf{e}_{j,1} + \epsilon_j\,\sin(\mathbf{k}_j\cdot\mathbf{r}-\omega_j t)\mathbf{e}_{j,2}], \quad j=1,2, \quad (8)$$

and where the field amplitudes $A_j^{(0)} = \omega_j\sqrt{I_j}(1+\epsilon_j^2)^{-1/2}$ are determined by their intensity I_j, the ellipticity $-1\leqslant\epsilon_j\leqslant 1$, as well as the frequency $\omega_j = 2\pi c/\lambda_j$ or the wavelength λ_j of the two modes. In the following, we choose the wave vectors $\mathbf{k}_j$ so that the first beam is directed with $\mathbf{k}_1 = \omega_1/c\;\mathbf{e}_z$ along the z axis, whereas the second beam propagates under the (crossing) angle δ with respect to the first beam with $\mathbf{k}_2 = \omega_1/c\;(\sin\delta\,\mathbf{e}_x + \cos\delta\,\mathbf{e}_z)$ within the $x-z$ reaction plane. This field configuration also accounts for a *standing* wave, if two beams with equal intensity and opposite helicity propagate under the angle $\delta = 180^\circ$ in just opposite directions. If the opening angle is small ($\delta\leqslant 5^\circ$), the modified Volkov phase $\Gamma(\boldsymbol{r},t)$ for such noncollinear beams can be written similarly to the single-beam case as

$$\Gamma(\mathbf{r},t) = \sum_{j=1}^{2}\left[\rho_{\epsilon,j}\,\sin\left(u_{\mathbf{k}_j}+\varphi_p^{(\epsilon_j)}\right) + \alpha_j^+\,\sin(2\,u_{\mathbf{k}_j}) - \alpha_j^-\,u_{\mathbf{k}_j}\right] + 2\,\alpha_{12}^+\,\sin\left(u_{\mathbf{k}_1}+u_{\mathbf{k}_2}\right) + 2\,\alpha_{12}^-\,\sin\left(u_{\mathbf{k}_1}-u_{\mathbf{k}_2}\right), \quad (9)$$

but where the various α coefficients now account for the simultaneous interaction of the atom with both beams. Again, the coefficients $\rho_{\epsilon,j}$, $\alpha_j^\pm$, and $\alpha_{12}^\pm$ have the same origin as in expression (6) and are given explicitly in Sec. 2 of the Appendix. Apart from the phase of the vector potentials, $u_{\mathbf{k}_j} = \mathbf{k}_j\cdot\mathbf{r}-\omega_j t$, moreover, the Volkov phase (9) now contains two terms that arise from both beams, $u_{\mathbf{k}_1}\pm u_{\mathbf{k}_2}$. These terms result from the contribution $\Gamma_3(\mathbf{r},t)$ in the general expression (4) and vanish identically if either of the two beam amplitudes $A_j^{(0)}$ is set to zero. These two nonlinear terms are also responsible for the cancellation of the Lorentz-force shifts for two not quite orthogonal beams as well as for the *virtual* Compton scattering of a standing-light wave [33]. The influence of the additional laser beam on the photoelectron phase can be seen readily in Fig. 2(c), whereas, for a fixed position $\mathbf{r}_o$, the time-harmonic dependence of the second beam gives rise to stronger oscillations of the amplitude around the ponderomotive phase with time. Furthermore, the different wave vectors of the two noncollinear beams lead to an additional directional dependence: The phase fronts in Fig. 2(f) are then tilted in the $x-z$ plane when compared to the single beam in Fig. 2(e).

Finally, a standing-light wave is obtained from the vector potential (7) if two counterpropagating plane-wave laser modes $\mathbf{A}^{(1,2)}(\mathbf{r},t)$ are assumed with equal intensity I and wavelength λ, but opposite sign of ellipticity $-1\leqslant\epsilon\leqslant 1$, in line with the two helicities $\Lambda=\pm 1$ of the circularly polarized components of the two beams. For such a superposition, the vector potentials can be written as

$$\mathbf{A}^{(1)}(\mathbf{r},t) = \frac{A_0}{\sqrt{1+\epsilon^2}}\,[\cos(kz-\omega t)\mathbf{e}_x - \epsilon\,\sin(kz-\omega t)\mathbf{e}_y],$$
$$\mathbf{A}^{(2)}(\mathbf{r},t) = \frac{A_0}{\sqrt{1+\epsilon^2}}[-\cos(kz+\omega t)\mathbf{e}_x + \epsilon\,\sin(kz+\omega t)\mathbf{e}_y],$$
$$\mathbf{A}_{-1}(\mathbf{r},t) = \mathbf{A}^{(1)}(\mathbf{r},t) + \mathbf{A}^{(2)}(\mathbf{r},t) = \frac{2A_0}{\sqrt{1+\epsilon^2}}\,\sin(kz)[\,\sin(\omega t)\mathbf{e}_x - \epsilon\,\cos(\omega t)\mathbf{e}_y],$$

where the wave number fulfills the standard dispersion relation $k=\omega/c$. Here we omit the explicit expression of the Volkov phase, which is readily obtained from Sec. 2 of the Appendix, if $\mathbf{k}_1 = -\mathbf{k}_2 = \mathbf{e}_z$ and $\epsilon_1 = -\epsilon_2 = \epsilon$ is entered into the modified Volkov phase (9).

C. Strong-field approximation amplitudes

We can directly make use of the Volkov solutions above for analyzing how the Lorentz force affects the ionization and recombination dynamics of electrons in quite different laser fields. In practice, this is most readily done in the SFA that has a number of advantages in describing the interaction of strong laser fields with simple quantum systems [22,34,35]. This approximation is valid especially for intense, low-frequency laser fields. Moreover, one often assumes a Keldysh parameter $\gamma < 1$, although this request is still under debate [36] and does not occur explicitly in the formal derivation. For such fields, the electron dynamics of the electron in the continuum is distorted only weakly by the (Coulomb) field of the residual ion and, hence, the influence of the atom can be described perturbatively. The SFA also provides an analytic formula for dealing with strong-field (ionization) processes, into which different physical interactions can be taken into account, such as the (distorted) Coulomb interaction of the outgoing electron with the ionic core or the nondipole interactions discussed above [37].

In the SFA, the angle- and energy-differential photoionization probability

$$P(\mathbf{p}) = p\,|\,T(\mathbf{p})\,|^2$$

is given in terms of the (square of the) transition amplitude $T(\mathbf{p})$, which, in turn, can be expressed as a sum of the (so-called) direct and rescattering amplitudes as

$$T(\mathbf{p}) = T^{(0)}(\mathbf{p}) + T^{(1)}(\mathbf{p}), \tag{10}$$

$$T^{(0)}(\mathbf{p}) = -i\int_{-\infty}^{\infty} d\tau\,\langle\chi_{\mathbf{p}}(\tau)|\,V_{le}(\mathbf{r},\tau)|\Psi_o(\tau)\rangle,$$

$$T^{(1)}(\mathbf{p}) = (-i)^2\int_{-\infty}^{\infty} d\tau\int_{\tau}^{\infty} d\tau'\langle\chi_{\mathbf{p}}(\tau')| \times V(\mathbf{r})U_{le}(\tau',\tau)V_{le}(\mathbf{r},\tau)|\Psi_o(\tau)\rangle, \tag{11}$$

in going from the initial state $\Psi_o(\mathbf{r},t) = \Phi_o(\mathbf{r})e^{+iI_p t}$ to the Volkov states $\chi_{\mathbf{p}}(\mathbf{r},t)$ of the outgoing electron. Indeed, this simple decomposition is independent of the spatial structure of the incident laser field and has a rather obvious physical interpretation: The (direct) amplitude $T^{(0)}(\mathbf{p})$ describes photoelectrons that are directly released from the target atom by the laser potential, $V_{le}(\mathbf{r},t)|\Psi_0\rangle$, and then *freely* propagate within the laser field as Volkov solution $\chi_{\mathbf{p}}$, until they reach the detector. In contrast, the rescattering amplitude describes those photoelectrons that are released as well by the laser potential, then evolve within the laser field by the time evolution $U_{le}(\tau',\tau)$ from time $\tau \to \tau'$, get rescattered by the potential $V(\mathbf{r})$ of the parent ion, before they also propagate towards the detector. This decomposition therefore enables one to account for the (magnetic) nondipole contributions into the direct and rescattering amplitudes by just applying the proper Volkov solution from above. This was first shown by Titi *et al.* [23] who explained the peak offset in the momentum distributions of ATI photoelectrons, and has recently been pursued further by us [26]. While the atomic potential $V(\mathbf{r})$ was originally neglected in the SFA in constructing the continuum states, Coulomb-Volkov waves or even distorted-Volkov waves can be applied quite readily to account for a proper atomic potential for the outgoing electron waves [13]. Indeed, the choice of this potential was found to be important especially for the low-energy part of ATI spectra [38], as well as for predicting the high-harmonic spectra for different driving laser beams in the optical and near-IR domain [39,40]. All these improvements in the evaluation of the transition amplitude given by (10) and (11) go well beyond the assumptions on which the SFA was built in the first place. Below, we shall especially focus on the direct amplitude (11) as the dominant term for all (direct) strong-field ionization processes.

D. Dipole approximation: Discarding the magnetic field

The direct amplitude (11) can be evaluated analytically if the *active* electron initially occupies a hydrogenic $1s$ state, and is scaled to the ionization potential of the target atom. For an elliptically polarized beam and within the electric-dipole approximation, i.e., $\mathbf{E}(\mathbf{r},t) \approx \mathbf{E}(t)$ and $\mathbf{B}(\mathbf{r},t) \approx 0$, the direct amplitude then takes the simple form

$$T^{(0)}(\mathbf{p}) = -2\pi i\,V(\mathbf{p})\sum_{n,m=-\infty}^{\infty}(-i)^m J_n\!\left(\frac{p_x A_0}{\sqrt{1+\epsilon^2}\omega}\right) \times J_m\!\left(\frac{\sqrt{1-\epsilon^2}p_y A_0}{\sqrt{1+\epsilon^2}\omega}\right)\delta(E_p + E_{nm}),$$

together with the matrix element of the Coulomb potential and the energies,

$$V(\mathbf{p}) = \langle\mathbf{p}|\,V(\mathbf{r})\,|\Phi_0\rangle = -\frac{2^{3/4}I_p^{5/4}}{\pi}\frac{1}{\frac{p^2}{2}+I_p}, \tag{12}$$

$$E_{nm} = -I_p - U_p + (n+m)\,\omega. \tag{13}$$

For the cases of either left- or right-circularly polarized light ($\epsilon = \pm 1$), moreover, this further simplifies with $E_n \equiv E_{n0}$ and $J_n(0) = \delta_{n,0}$ to

$$T^{(0)}(\mathbf{p}) = -2\pi i\,V(p)\sum_{n=-\infty}^{\infty}(-1)^n J_n\!\left(\frac{p_x A_0}{\sqrt{2}\,\omega}\right)\delta(E_p + E_n). \tag{14}$$

As seen from expansion (14), the transition amplitude $T^{(0)}(\mathbf{p})$ comprises the energy spectrum of the ATI photoelectrons in terms of a sum of discrete δ-like peaks. The position of these ATI peaks hereby ensures energy conservation of the ATI process owing to the absorption of a well-defined number of photons. For circularly polarized light, therefore, the possible photoelectron energies at the detector are just given by

$$E_p = -I_p - U_p + n\,\omega,$$

e.g., photoelectrons are observed only if the atom absorbs n photons with $n\,\omega > I_p + U_p$. In addition, the prefactors of the δ function in the transition amplitude (14) determine the line strengths of the ATI peaks and give rise to the probabilities

$$P_n(\mathbf{p}) = (2\pi)^2\sqrt{E_p}\,V(\sqrt{2E_p})\,J_n^2\!\left(\frac{\sqrt{2\,E_p}A_0}{\sqrt{2}\,\omega}\right).$$

With these probabilities, the ATI spectrum just extends up to the cutoff $n_{\max}$, simply because the Bessel function behaves

asymptotically as $J_n(x) \sim e^{-n}$ for $n > x$. Here, we shall not display an explicit expression for this cutoff parameter, but only note that it can be approximated quite well by the classical formula $n_{\max} = \sqrt{2\,U_p/\omega}$. For typical laser parameters ($\lambda = 800$ nm and $I \approx 10^{14}$ W/cm^2), this cutoff lies in the order of $n \simeq 10$, so that the maximum photoelectron energy in direct ATI spectra appears at about 12–15 eV. For the energy spectra of direct photoelectrons, in addition, the length gauge has been found to be superior for nonspherical initial states [41]. From a large number of weak fields, however, it is known that such a simple *rule* does not apply for most, much less *all* ionization or capture processes [42], and a similar behavior is therefore also expected for strong-field ionization processes.

E. Nondipole approximation: Working with spatially dependent electric fields

The magnetic field enters the traditional SFA mainly via the Volkov(-type) solution on the left-hand side of both the direct and/or rescattering amplitudes for different field configurations. Several lengthy expressions have been derived for various superpositions in order to quantitatively understand the Lorentz-force contributions to selected strong-field ionization and rescattering processes.

For the sake of simplicity, let us restrict ourselves to just a single elliptically polarized beam, for which the direct amplitude becomes

$$T^{(0)}(\mathbf{p}) = -2\,\pi\,i \sum_{n,m=-\infty}^{\infty} J_n(\rho_\epsilon) J_m\left(\alpha \frac{1-\epsilon^2}{1+\epsilon^2}\right) V(\mathbf{p}_{nm})\; e^{i\,n\,\varphi_p^{(\epsilon)}} \times \delta[E_p + \tilde{U}_p + I_p - (n+2\,m)\,\omega_0], \tag{15}$$

with the matrix element (12), the parameters from above, and the kinetic momenta of the electron in the (nondipole) laser field,

$$\mathbf{p}_{nm} = \mathbf{p} + [\tilde{U}_p/\omega_0 - (n+2\,m)]k_0\;\mathbf{e}_z. \tag{16}$$

The possible values of these momenta (16) can be obtained from the Volkov phase (6) by applying a Jacobi-Anger expansion with regard to $e^{-i\,\Gamma(\mathbf{r},t)}$; they clearly indicate that the photoelectron absorbs $(n+2\,m)$ photons from the nondipole laser field. The two parts to this photon number result from the contributions $\Gamma_1(\mathbf{r},t)$ and $\Gamma_2(\mathbf{r},t)$ of the total Volkov phase in Eq. (4) and correspond in the dipole limit to the two terms $\mathbf{p}\cdot\mathbf{A}$ and $\mathbf{A}^2$ in (2). Because of the Lorentz force, moreover, the kinetic momentum of the electron gains an additional component $[\,\tilde{U}_p/\,\omega_0 - (n+2\,m)\,]\,k_0\,\mathbf{e}_z$ along the beam axis owing to the (magnetic) ponderomotive contribution as well as the discrete numbers of photon momenta $\hbar k_0$. All these momenta are "absorbed" from the magnetic part of the laser field. Equation (16) therefore also exhibits the momentum conservation in the ATI process that is not present in the dipole approximation.

Of course, Eqs. (15) and (16) contain, as a special case for $\epsilon = 1$, a (single) circularly polarized beam. Making use of the identity $J_m(0) = \delta_{m,0}$, the summation over m can be dropped from the transition amplitude (15) and the outcome compared to the dipole amplitude (14). This comparison shows that the nondipole interaction gives rise to a shift of the photoelectron momentum along the z axis, in addition to the (dipole) shift of the photoelectron energy as it becomes visible in the ATI peaks. In other words, any absorption of a photon from the field not only leads to a peak shift in the energy spectrum, but also to a change of photoelectron momentum along the beam axis by $\hbar k_0$. Classically, this means that the electron will be accelerated along the beam axis, which is possible only by a magnetic field or the combination of electric and magnetic fields. This is indeed in contrast to the dipole approximation, in which the momentum of the photoelectron is *conserved* since the laser field $\mathbf{A}(t) \neq \mathbf{A}(\mathbf{r},t)$ does not carry any linear momentum itself.

Finally, the basic form of the direct amplitude (14) remains the same even if several nonparallel beams are considered. For such a field configuration, each beam contributes a double summation for its own as well as an additional term in the δ function owing to the fundamental frequency ω_i and the first overtone $2\,\omega_i$, respectively. The same decomposition can also be made for the modified momenta in the laser field where each beam gives an analog term to the amplitude along its propagation direction $k_i\,\boldsymbol{e}_i$, since the photon energies and momenta always appear together in the phase $u_{\mathbf{k}_0}$.

III. LORENTZ-FORCE SHIFTS TO ATOMIC STRONG-FIELD PROCESSES

A. Peak shifts of electron momenta in ATI spectra

Contributions of the Lorentz force to the strong-field ionization of atoms and molecules were first observed in the momentum distribution of the emitted photoelectrons. Instead of (strictly) following the electric field vector $\boldsymbol{\mathcal{E}}$ perpendicular to the laser propagation, small shifts of the electron momenta either along or opposite to the laser propagation have been recorded for different gas targets. These shifts depend on the intensity, the wavelength, and weakly also upon the polarization of the beam, although here we shall restrict our discussion to just circularly polarized beams. Such longitudinal peak shifts of the electron momenta will also suppress, of course, the intensities of the high harmonics and then require further experimental measures in order to make HHG with a mid-IR field feasible.

For mid-IR driving fields, in particular, a nonzero p_z component of the photoelectron momenta along the propagation direction of the laser was found in various strong-field ionization experiments [19–21], a phenomenon that is nowadays briefly known as *peak shift* Δp_z in the literature. In a pioneering work, Smeenk *et al.* [43] first measured the momentum distribution in the $x-z$ plane with circularly polarized driving laser fields of different intensity at 800 and 1400 nm and by applying velocity map imaging. In these measurements, peak shifts $\Delta p_z = 5, \ldots, 20 \times 10^{-3}$ a.u. were found at these wavelengths, which correspond to about $5, \ldots, 10$ photon momenta, and which increased linearly with the laser intensity. This behavior also follows the classical expectation $\beta_o \propto I\,\lambda^3$ as discussed in Fig. 1, while more accurate and reliable measurements of the λ dependence still remain a major technical challenge [21,44].

For a purely linearly polarized, single-mode laser pulse ($\epsilon = 0$), the energy conservation due to the δ function in

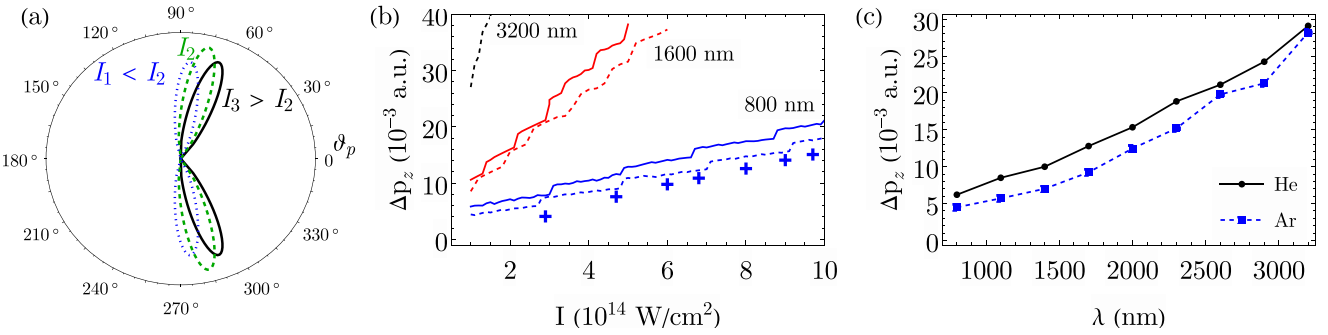

FIG. 3. Peak shifts of the photoelectron momentum distributions in the ATI of neutral gas targets, if driven by a single circularly polarized plane-wave laser beam along the z axis. (a) Schematic PAD of the photoelectrons for three different beam intensities with $I_1 < I_2 < I_3$. The Lorentz force pushes the electrons along the propagation direction and, thus, tilts the angular distributions in the $x-z$ plane towards the beam axis (exaggerated in this figure). This tilt increases roughly linearly with the beam intensity, as discussed in Sec. III A. (b) Peak shift $\Delta p_z = E_{p,\max} \cos \vartheta_{\max}$ as a function of beam intensity. Shifts are shown for three different wavelengths with $\lambda = 800$ nm (blue lines), 1600 nm (red lines), and 3200 nm (black line), as well as for helium (solid lines) and argon (dashed lines) targets, respectively. The peak shift refers to those ATI peak, for which the maximum ionization probability occurs at the modulus $p = \sqrt{2\,E_{p,\max}}$, $\vartheta_{p,\max}$, and $\varphi = 0$ of the photoelectron momentum in the $x-z$ plane. (c) The same peak shift Δp_z, but as function of the wavelengths of the incident beam for helium (solid line) and argon (dashed line) targets and at fixed intensity $I = 10^{14}$ W/cm^2. See text for further discussions.

Eq. (15) leads to

$$E_p + \frac{U_p}{1 - \sqrt{2\,E_p}\cos\vartheta_p/c} + I_p - (n + 2\,m)\omega_o = 0. \quad (17)$$

This conservation ensures that the energy of any discrete ATI peak at polar angle ϑ_p solely depends on two integers n and m, while their strength is given by the prefactor in Eq. (15). Analog arguments can be used for a circularly polarized (single-mode) laser pulse, for which the δ function in Eq. (15) leads to less ATI peaks at the energies,

$$E_p + \frac{U_p}{1 - \sqrt{2\,E_p}\cos\vartheta_p/c} + I_p - n\,\omega_o = 0,$$

but which agree with those for linearly polarized light if $m = 0$. In Ref. [26], we have computed such ATI photoelectron spectra for various noble-gas atoms and mid-IR plane-wave laser beams. These computations clearly demonstrated that the peak shifts in the p_z direction can be readily extracted from the nondipole laser-electron interaction [45].

Figure 3 shows the peak shifts in the ATI photoelectron momentum distributions for selected gas targets. These distributions are displayed schematically in Fig. 3(a) as a function of the polar angle and for three beam intensities, $I_1 < I_2 < I_3$. Since the Lorentz force pushes the electrons along the propagation direction, the PADs are tilted towards the beam axis, although quite exaggerated in this figure. Apart from these PADs, Fig. 3(b) reveals a (nearly) linear dependence of the peak shift $\Delta\,p_z$ upon the (peak) intensity, in line with the classical theory, in which the Lorentz force $F_z \sim I\,\lambda$ exerts a peak shift $\Delta p_z \sim I\,\lambda^2$. As seen from Fig. 3(b), however, the calculated peak shifts $\Delta\,p_z$ are always larger than the measured values. This difference can be explained by the following two reasons: (i) For an infinite pulse, the constant intensity in time is larger than the temporally averaged intensity of finite pulses, as they were applied experimentally. (ii) For real pulses, furthermore, a counteracting Lorentz-force contribution arises from the gradient of the spatial envelope, when compared with an infinitely extended plane-wave beam. If both these temporal and spatial dependencies are taken into account by a (so-called) focal averaging, they result in a peak shift that is always smaller than those for constant intensities [23,43].

Apart from the overall linear behavior of Fig. 3(b), the peak shift $\Delta\,p_z$ exhibits a stepwise structure with small but regular jumps in p_z. These steps can be understood from the (infinitely long) *continuous* driving beam, as assumed in our computations, and for which the energy spectra always consist of discrete δ-like ATI peaks, well separated from each other by the photon energy $\hbar\,\omega$. Thus, the peak shift, i.e., the maximum momentum along the beam axis, needs to be obtained in Fig. 3(b) for a particular ATI peak, $E_{p,\max} = E_{p,N}$, with maximum ionization strength and which moves to the neighbored ATI peak, $E_{p,\max} = E_{p,N+1} \approx E_{p,N} + \hbar\,\omega$, if the laser intensity has been sufficiently increased. This jump in $\Delta\,p_z$ is also seen from its dependence $\Delta p_z = \sqrt{2E_{p,\max}}\cos\vartheta_{p,\max}$ upon the maximum energy of the photoelectrons, $E_{p,\max}$. Figure 3(c) finally displays the peak shift Δp_z as a function of the wavelengths of the incident beam for a helium (solid lines) and argon (dashed lines) target. While these shifts increase roughly linearly with λ, accurate measurements on this wavelength dependence are quite difficult to perform and likely require further advances in the velocity mapping in order to confirm or deny our predictions based on SFA and the nondipole Volkov states (6).

B. Steering the electron momenta with noncollinear laser beams

While the Lorentz force above, as it arises from the direct amplitude (15), always shifts the electron momenta in a forward direction with regard to the beam propagation, a *backward* shift may arise for a sufficiently strong rescattering of the emitted electrons. While momentum conservation generally requires a transfer of the absorbed photon momentum to both the emitted electron and its parent ion, the details of this (momentum) sharing are still not well understood. From a simplified viewpoint, this momentum transfer may happen in the course of the tunnel ionization barrier and may lead

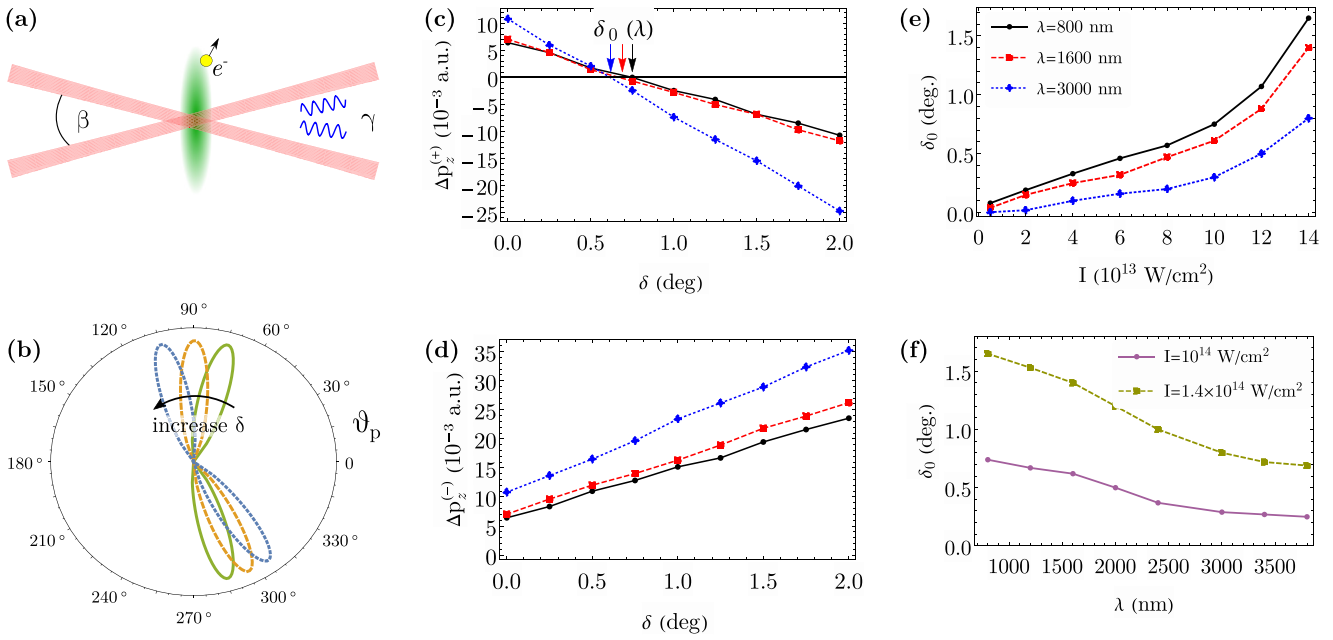

FIG. 4. Peak shifts of the photoelectron momentum distributions in the ATI of neutral gas targets if driven by noncollinear beams. (a) Two not quite collinear infrared beams (red) with opening angle δ as well as with equal intensity and polarization may help enhance the rescattering of photoelectrons with their parent ions. The interaction of these beams with an atomic gas target gives rise to either the emission of ATI photoelectrons (yellow) or high harmonic photons (blue). (b) For two such noncollinear beams, the Lorentz force always shifts, analogously to Fig. 3, the peak of the photoelectron momentum distributions into the forward direction (green-solid distribution), if the opening angle δ is sufficiently small. For an increasing angle, however, a good fraction ($\lesssim$0.5) of the photoelectrons returns within the polarization plane (orange-dashed distribution for $\vartheta = 90^\circ$, though exaggerated in this drawing) and may thus facilitate the recombination with the parent ion. If the opening angle δ is enlarged further, a peak shift along the negative z axis occurs for photoelectrons in the upper half ($90^\circ \leqslant \vartheta \leqslant 180^\circ$), while the photoelectrons in the lower half are shifted even further away from the polarization plane (blue-dotted distribution). The peak shifts of the ATI photoelectron are also shown also as function of the opening angle in the (c) upper and (d) lower halves of the $x-z$ plane. Results are displayed for circularly polarized beams ($\epsilon = \pm 1$) with intensity $I = 10^{14}$ W/cm^2 and for the three wavelengths $\lambda = 800$ nm (black solid lines), $\lambda = 1600$ nm (red dashed lines), and $\lambda = 3200$ nm (blue dotted lines). For the *optimal* opening angle δ_0, there occurs a *zero* peak shift in the upper half plane. (e) Optimal opening angle as a function of the laser intensity and for the same wavelengths as in (c) and (d). (f) The same but as a function of the wavelength and shown for two intensities, $I = 5 \times 10^{13}$ W/cm^2 (green-dashed line) and $I = 10^{14}$ W/cm^2 (purple-solid line). All these data were generated for an argon target with ionization potential $I_p = 15.76$ eV and photoelectron energy $E_p = 8.1$ eV $\approx 5.2\,\omega$ at the maximum of the momentum distribution.

to backward shifts, as observed for linearly polarized beams [19].

To partly counteract the forward shift of the electron momenta by the Lorentz force, a superposition of (two) not quite collinear laser pulses has been considered by us following an earlier semiclassical argumentation by Pisanty *et al.* [46]. These arguments were originally based on the local forward ellipticity of the total electric field in the interaction region, which returns a part of the electron wave packet back to the parent ion, while other parts are shifted even further away. However, this discussion of the electric field alone neglects the contributions of the magnetic field. Below, we therefore first analyze the ATI for two not quite collinear laser beams with the same wavelength, intensity, and ellipticity by using the nondipole SFA from Sec. II C. In particular, here we wish to understand how the energy spectra and PAD of the photoelectrons depend on the opening angle δ of the two crossed beams, and as it is shown schematically in Fig. 4(a).

For two noncollinear beams, we found in Sec. II B that the nondipole SFA theory gives rise to the modified Volkov phase (9), in which the photoelectron acquires individual phase contributions from the two laser beams, but also due to the simultaneous interaction with both beams together (mixed terms). If we insert the Volkov phase (9) into the direct SFA (11) transition amplitude, we obtain

$$T^{(0)}(\mathbf{p}) = -2\pi i \sum_{N_1,N_2=-\infty}^{\infty} C_N(\mathbf{p}) V(\mathbf{p}_N) \delta(E_N + I_p),$$

$$E_N = E_p + \tilde{U}_{p,1} + \tilde{U}_{p,2} - N_1\,\omega_1 - N_2\,\omega_2, \qquad (18)$$

$$\mathbf{p}_N = \mathbf{p} + \frac{\tilde{U}_{p,1}}{\omega_1}\mathbf{k}_1 + \frac{\tilde{U}_{p,2}}{\omega_2}\mathbf{k}_2 - N_1\mathbf{k}_1 - N_2\mathbf{k}_2, \qquad (19)$$

where the δ function still indicates the position of the discrete ATI peaks in the energy spectrum. The relative amplitudes of these peaks are determined by the coefficients $C_N(\mathbf{p})$ as well as the matrix element $V(\mathbf{p}) = \langle \mathbf{p}|\, V(\mathbf{r})\, |\Psi_o\rangle$ of the active electron for undergoing a transition into the continuum due to the atomic potential $V(\mathbf{r})$. Moreover, the integers N_1 and N_2 refer to the number of photons as absorbed from the two laser modes. This direct amplitude therefore gives rise to an ionization probability that describes ATI peaks owing to the absorption of photons from both laser modes, but where the

exact positions of the peaks depend on the opening angle of the two driving beams.

For two not quite orthogonal beams, Fig. 4(b) clearly shows that the Lorentz force always shifts the peaks of the photoelectron momentum distribution into the forward direction (green-solid distribution), if the opening angle δ is just sufficiently small. This is rather analogous to a single beam, as discussed in Sec. III A; cf. Fig. 3. However, when the opening angle δ of the two beams increases, some fraction ($\lesssim$0.5) of the photoelectrons may return back within the polarization plane (i.e., at $\vartheta_p = 90^\circ$, orange-dashed distribution) and thus facilitate a recombination with the photo-ion. For two noncollinear beams, therefore, an *optimal* opening angle δ_0 *does* exist such that a maximum number of electrons return to their parent ions. At this optimal angle δ_0 for the crossing of these beams, the electrons from the upper half of the PAD ($90^\circ \leqslant \vartheta_p \leqslant 180^\circ$) will remain within or near to the polarization plane. By using the nondipole Volkov states (9) in the direct SFA amplitude, indeed, such a rotation of the PAD is found for all photoelectron energies which significantly contribute to the ATI spectrum.

Figures 4(c) and 4(d) show the peak shifts of the photoelectron momentum distributions in the ATI as a function of the opening angle in the upper [Fig. 4(c)] and lower [Fig. 4(d)] halves of the $x-z$ plane. This peak shift decreases for all photoelectrons in the upper half with $0^\circ \leqslant \vartheta \leqslant 180^\circ$, while it becomes even larger for the electrons from the lower half. In these figures, the results are shown for circularly polarized beams ($\epsilon = \pm 1$) with intensity $I = 10^{14}$ W/cm^2 and for the three wavelengths $\lambda = 800$ nm (black-solid line), $\lambda = 1600$ nm (red-dashed line), and $\lambda = 3000$ nm (blue-dotted line), respectively. For the *optimal* opening angle δ_0, there occurs (by definition) a *zero* peak shift in the upper half plane. Figure 4(e) displays this optimal opening angle as a function of the laser intensity and for the same wavelengths as in Figs. 4(b) and 4(c). The same optimal angle, though as a function of the wavelength, are finally shown in Fig. 4(f) for two selected intensities, $I = 10^{14}$ W/cm^2 (purple-solid line) and $I = 1.4 \times 10^{14}$ W/cm^2 (green-dashed line). All of these dependencies clearly show that a proper choice of the opening angle between the two incident beams may also support an efficient HHG with mid-IR laser beams.

C. Kapitza-Dirac effect in standing-light fields

In 1933, Kapitza and Dirac suggested that free electrons should be deflected by an intense and perpendicular-oriented standing-light wave owing to the absorption of photons from the two counterpropagating laser modes [47]. In standing waves, in particular, electrons may absorb a photon from one mode and reemit it subsequently into another mode, a process known as *virtual* Compton scattering [48]. Since both modes have the same wavelength (photon energy), the electron energy remains the same in this process, while its momentum changes by $2\hbar\mathbf{k}$. This momentum change then leads to a characteristic deflection of the electrons with momentum components along the optical axis. Measurements of this (low-intensity) Kapitza-Dirac effect (KDE) have remained a challenge until now because typically only a few photon momenta $\hbar k$ are exchanged [49–51].

In contrast, a much larger momentum transfer normally occurs in high-intensity standing fields owing to the multiple interaction of the electrons with the radiation field. This enhanced momentum transfer was first observed by Bucksbaum *et al.* [52] who, instead of a free-electron beam, placed neutral atoms within the standing wave and measured the ATI photoelectrons. While these electrons are first released within a rather narrow spatial region near to the polarization plane, and separated by $\hbar\omega$ in energy from each other, they may become multiply scattered in the continuum and then reach the detector with longitudinal momenta up to the order $1000\,\hbar k$.

Figure 5 outlines the behavior of the high-intensity KDE in an intense standing-light wave. In a typical setup, neutral atoms are placed at $z = z_0 \neq n\lambda/2$ in an intense standing wave and emit ATI photoelectrons that are measured with momentum $\mathbf{p} = (p, \vartheta_p, \varphi_p)$ at the detector D; cf. Fig. 5(a). Typical spectra $P(E_p) \equiv P(\sqrt{2E_p}, \vartheta_p = \text{const}, \varphi_p = 0)$ are shown in Fig. 5(b) for two selected values of the polar angle ϑ_p and the fixed azimuthal angle, $\varphi_p = 0$. Figure 5(c) displays the PAD $P(\vartheta_p) \equiv P(\sqrt{2E_{p,0}}, \vartheta_p, \varphi_p = 0)$ at fixed energy $E_{p,0}$ and $\varphi_p = 0$ and, hence, just counts the electrons as a function of ϑ_p. These PADs are shown for high-energetic (green-solid curves) and low-energetic (blue-dashed curves) photoelectrons. In these PADs, two distinct scattering regimes can be distinguished for sufficiently weak standing fields by the ponderomotive energy U_p and, hence, the energy $E_p = p^2/2$ of the emitted photoelectrons. In the so-called Bragg regime, rather high-energetic electrons ($E_p \gg U_p$) are deflected according to Bragg's law $n\lambda_e/\lambda = 2\sin\vartheta$ with the de Broglie wavelength $\lambda_e = h/p$ of the detected electrons. This Bragg's law can be readily understood in terms of the classically ponderomotive force $\boldsymbol{F}_p$. For a standing-light wave, this force points along the beam axis and has a spatial periodicity of $\lambda/2$, i.e., it forms a well-known Bragg grating. For an electron that impinges with momentum p and de Broglie wavelength $\lambda_e = h/p$ on the standing wave, a *grating* is formed by the minima and maxima of F_p.

In the diffraction regime ($E_p \ll U_p$), in contrast, a deflection pattern is formed behind the standing wave due to the multiple absorption and emission of photons. Qualitatively, the momentum transfer in such a multiple scattering of photons can be derived by again analyzing the direct SFA amplitude (11) for two counterpropagating laser beams with opposite helicity. In practice, this amplitude takes a form similar to (18),

$$
\begin{aligned}
T^{(0)}(\mathbf{p}) &= -2\pi i \sum_{N_1,N_2,N_{12}-\infty}^{\infty} C_N(\mathbf{p})\, V(\mathbf{p}_N)\, \delta(E_N + I_p), \\
E_N &= E_p + 2\tilde{U}_p - (N_1 + N_2)\,\omega, \\
\mathbf{p}_N &= \mathbf{p} + \frac{2\tilde{U}_p p_z}{c\,\omega}\mathbf{k} - (N_1 - N_2)\mathbf{k} - 2N_{12}\mathbf{k},
\end{aligned}
\tag{20}
$$

as discussed above for two noncollinear beams. When compared with Eqs. (18) and (19), however, additional terms appear, each in the energy E_N as well as the momenta $\mathbf{p}_N$ of the photoelectrons owing to the absorption of photons from one and the reemission into the second mode, i.e., the *virtual* Compton scattering from above [33]. This Compton scattering leads to a momentum transfer or peak shift Δp_z along the

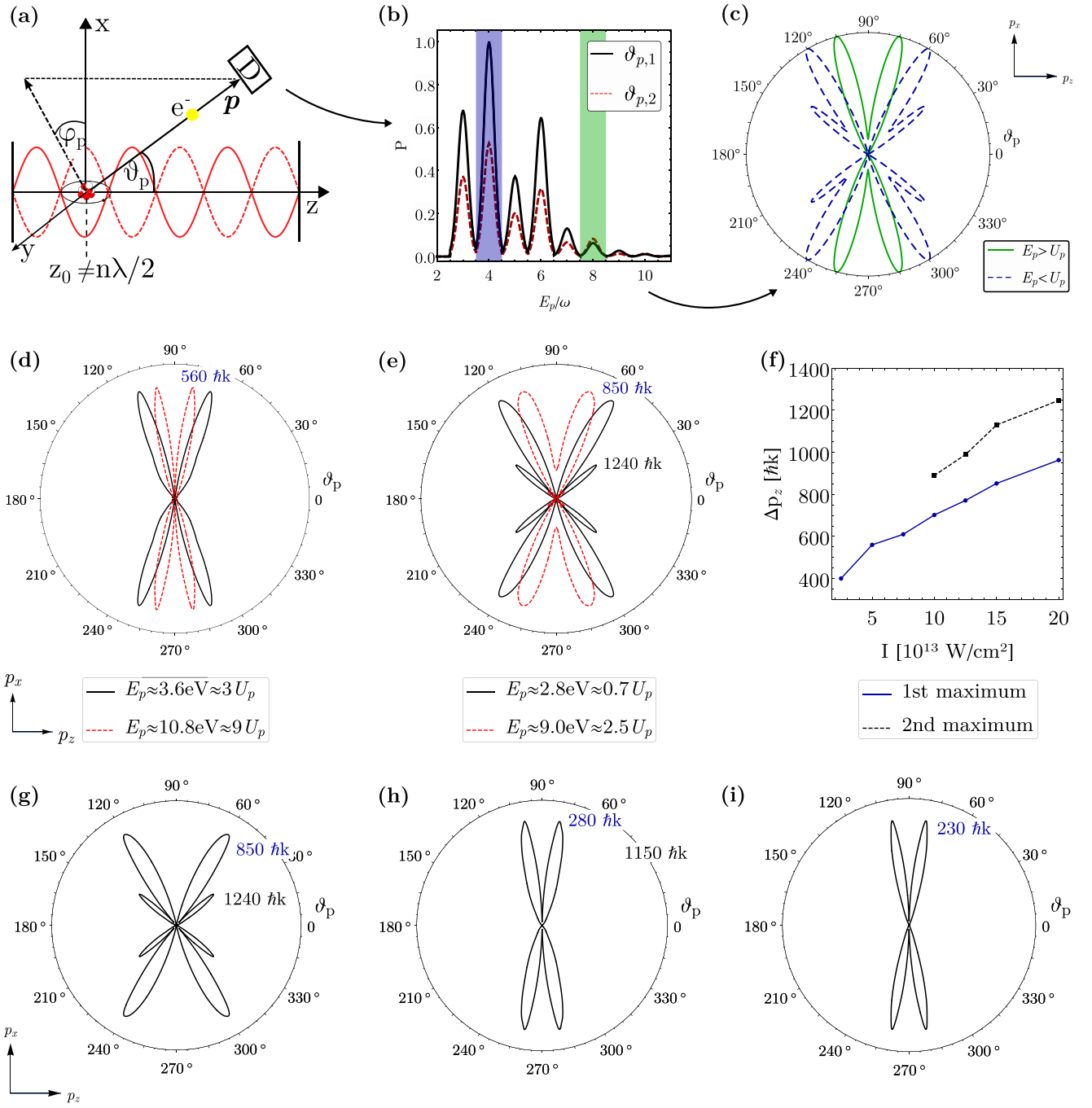

FIG. 5. High-intensity Kapitza-Dirac effect (KDE) with neutral atoms in an intense standing-light field. (a) In a typical setup, neutral atoms are placed at $z = z_0 \neq n\,\lambda/2$ in an intense standing wave and emit ATI photoelectrons that are measured with momentum $\mathbf{p} = (p, \vartheta_p, \varphi_p)$ at the detector D. (b) Typical photoelectron energy spectrums $P(E_p) \equiv P\,(\sqrt{2\,E_p}, \vartheta_p = \text{const}, \varphi_p = 0)$ for two selected values of the polar angle ϑ_p (black-solid and red-dashed curves), but at fixed azimuthal angle, $\varphi_p = 0$. For any selected ATI peak at energy $E_{p,0}$, the PAD $P(\vartheta_p) \equiv P\,(\sqrt{2\,E_{p,0}}, \vartheta_p, \varphi_p = 0)$ just counts the electrons as a function of ϑ_p. (c) Typical PAD of high-energetic (green-solid curves) and low-energetic (blue-dashed curves) photoelectrons. (d),(e) PADs are shown for photoelectrons with energy $E_p \approx 3\,\omega$ (black-solid lines) and $E_p \approx 10\,\omega$ (red-dashed lines) for laser intensities (d) $I = 5 \times 10^{13}$ W/cm^2 and (e) $I = 15 \times 10^{13}$ W/cm^2, respectively. (f) Peak shifts $\Delta p_z = \sqrt{2\,E_p}\cos\vartheta_{p,\max}$ due to momentum transfer to photoelectrons with energy $E_p \approx 3\,\omega$ as a function of intensity, and taken at the maximum strength of the PAD. (g),(h) PAD of low-energy photoelectrons with $E_p = 2.8$ eV $\approx 0.7\,U_p$ for (g) linear, (h) elliptical, and (i) circular polarizations of the standing-light wave. Results are shown for $I = 15 \times 10^{13}$ W/cm^2 (black-solid curves) of the counterpropagating laser modes. All PADs have been normalized upon their maximum. In (d)–(i), moreover, a laser beam with $\lambda = 1200$ nm ($\omega = 1.03$ eV) and a krypton target with $I_p = 14$ eV were assumed, analogous to Ref. [52].

beam axis for each ATI peak and, hence, to a deflection of the photoelectrons in the high-intensity KDE. We note that such a transfer is possible only because of the antiparallel $\mathbf{k}_{1,2}$ vectors of the counterpropagating modes and their identical wavelengths.

Until now, only the high-energetic photoelectrons ($E_p > U_p$) have been observed and analyzed for the high-intensity KDE, comparable to the Bragg regime with a free electron at low intensities. Moreover, only standing waves of linear and circular polarizations were considered experimentally. However, since standing-light waves with elliptical polarization and high intensity can nowadays be generated quite routinely, measurements of low-energy photoelectrons with $E_p < U_p$ and just a (very) few virtual Compton scattering processes will become feasible and will then result in a pattern of low diffraction order.

Figure 5(d) displays the PAD of photoelectrons with energies $E_p \approx 3\,\omega$ (black-solid lines) and $E_p \approx 10\,\omega$ (red-dashed lines) for the laser intensity $I = 5 \times 10^{13}$ W/cm^2. For a linearly polarized standing wave ($\epsilon = 0$) and intensity $I = 5 \times 10^{13}$ W/cm^2, the photoelectrons are emitted preferably with the momentum transfer $\Delta p_z \approx 560\,\hbar k$, as seen by the four maxima in the PAD. These maxima occur symmetrically with regard to the polarization plane ($\vartheta = 0^\circ$) and are split into two peaks in the upper (lower) half due to the nondipole contributions to the amplitude (20) These four maxima all have a similar shape, independent of the photoelectron energies E_p, while the angle $\vartheta_{\max}$ of the maximum photoelectron emission decreases with E_p.

At the higher laser intensity $I = 15 \times 10^{13}$ W/cm^2 in Fig. 5(e), the four maxima in the PAD of high-energetic photoelectrons are still clearly discernible, but now occur for a predominant momentum transfer of $\Delta p_z \approx 850\,\hbar k$. Here, however, a markedly different PAD is found for the low-energy photoelectrons ($E_p < U_p$) with momentum transfer $\Delta p_z \approx 1240\,\hbar k$. The different behavior of the PAD for low- and high-energy photoelectrons can be understood in terms of the Lorentz force that acts on the photoelectron in a standing-light wave. In the three-step model of strong-field ionization, the photoelectrons leaves the atom with a velocity vector parallel to the polarization direction (x axis) of the standing wave. The (magnetic) Lorentz force then induces an oscillating motion along the beam axis. As in the free-electron KDE, the motion of the photoelectron is not bounded for $E_p > U_p$ by the ponderomotive potential and can thus be described classically, leading to a distinct value of the longitudinal momentum Δp_z measured at the detector [52]. For $E_p < U_p$, on the other hand, the photoelectron can classically not move beyond the crests of the ponderomotive potential. Moreover, the plane-wave contributions with different Δp_z in its wave function interfere and give rise to other (sets of) maxima in the PADs. Within the SFA, these contributions arise from and are associated to different terms of the nondipole Volkov states. For the photoelectrons with energy $E_p \approx 3\,\omega$, Fig. 5(f) displays the peak shifts $\Delta p_z = \sqrt{2\,E_p}\cos\vartheta_{p,\max}$ as a function of intensity and taken at the maximum strength of the PAD.

Figures 5(g)–5(i) finally display the PAD of the low-energetic photoelectrons with $E_p = 2.8$ eV $\approx 0.7 U_p$ for linear [Fig. 5(g)], elliptical [Fig. 5(h)], and circular [Fig. 5(i)] polarizations of the standing-light wave. Results are shown again for the intensity $I = 15 \times 10^{13}$ W/cm^2 (black-solid curves) of the two counterpropagating laser modes. As seen from this figure, the momentum transfer to the low-energetic photoelectrons can be enhanced significantly [when compared to the blue-dashed curve in Fig. 5(c)] by simply controlling the polarization of the standing wave.

D. High-harmonic generation: Missing the recombination at long wavelengths

High harmonics typically refer to coherent light at multiples of the fundamental laser frequency that are generated when an (atomic) gas target is irradiated by an *intense* laser of, say, $I \gtrsim 10^{13}$ W/cm^2. The generation of such harmonics is a nonlinear (optical) up-conversion process, for which the conservation of energy, linear momentum, as well as spin and orbital angular momentum of individual harmonics can often be expressed by means of rather simple selection rules [53,54]. In applications, the high harmonics are usually generated with linearly polarized beams since the return to and the recombination of the electron with its parent ion is crucial for the HHG mechanism, and where the yield rapidly decreases for elliptically polarized laser pulses as the ellipticity $\epsilon \to \pm 1$. For optical and near-IR laser pulses, nevertheless, this laser-driven recollision mechanism of electrons has led to photon energies several tens of times larger than the driving laser frequency.

Great efforts have been undertaken in the past in order to increase the efficiency of HHG. For a given laser beam with ponderomotive potential $U_p = I/4\,\omega_o^2$, the generated spectrum of harmonics can often be separated into two regions: (i) the plateau of harmonics with photon energies below $I_p + 3.17\,U_p$ and rather constant yields, and (ii) the harmonics of higher energy but with a rapidly decreasing yield. The quite simple design of HHG experiments makes it then desirable to extend the plateau towards the x-ray regime by just following the cutoff law $\hbar\,\omega_{\max} = I_p + 3.17\,U_p$ and, hence, by increasing U_p. At first glance, this desire appears to be easily fulfilled since the ponderomotive energy $U_p \propto I\,\lambda^2$ is found proportional to the intensity I and the (square of) wavelength λ of the laser field. For mid-IR beams, however, the yield of energetic photons is already markedly suppressed by the Lorentz force. In practice, therefore, any increase of the cutoff photon energy generally lowers the radiation yield and renders the HHG process unattractive as an x-ray light source.

Analogous to Sec. III B above, a superposition of noncollinear beams may offer a way out of this limitation as it counteracts the Lorentz force and may bring a sizable fraction of electrons back to their parent ions. To understand the most favorable opening angle δ_o of the two incident beams, here one needs to analyze how the nondipole Volkov states contribute to the *rescattering* amplitude. In contrast to the ATI from above, however, this amplitude must first be expressed in terms of the harmonic dipole moment,

$$\mathbf{D}(t) = -\,i \int_{-\infty}^{t} dt' \int d^3\mathbf{p}\; e^{-iI_p t}\mathbf{d}^\dagger[\mathbf{p} + \mathbf{A}(\mathbf{r}, t)] \times \mathbf{E}(\mathbf{r}, t) \cdot \mathbf{d}[\mathbf{p} + \mathbf{A}(\mathbf{r}, t')] + \text{c.c.}, \tag{21}$$

which describes the *recombination* of the returning electron with the parent ion in terms of the (dipole) matrix elements

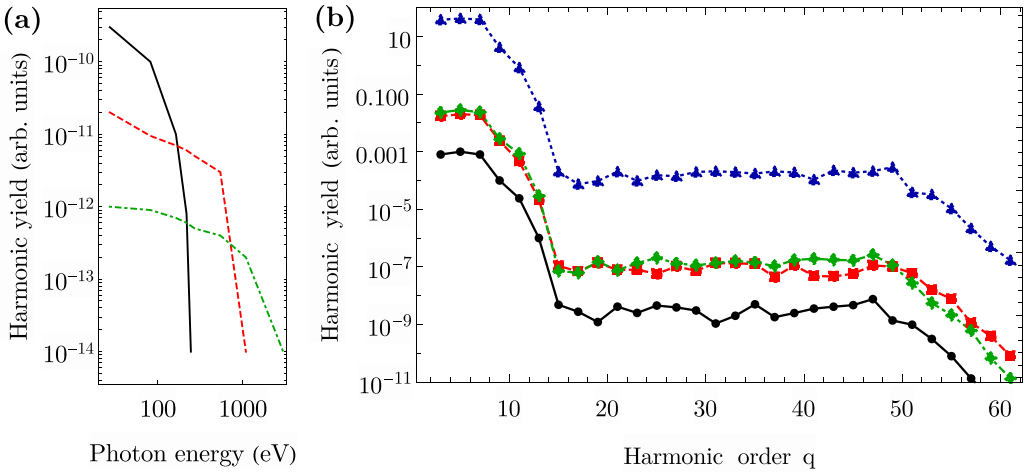

FIG. 6. HHG in intense near- and mid-IR laser fields. (a) For a single IR laser beam, the yield of the high harmonics is strongly suppressed because of the Lorentz force that pushes the electron away from its parent ion. The envelopes of HHG spectra are shown for 800 nm (black-solid curve), 2000 nm (red-dashed curve), and 4000 nm (green dot-dashed curve). The HHG spectra were computed for He^+ target ions and the intensity $I = 10^{15}$ W/cm^2. (b) HHG spectra for two not quite collinear beams, but with different opening angles $\delta = 0.2^\circ < \delta_0$ (red-dashed curve), $\delta = 0.75^\circ \approx \delta_0$ (blue-dotted curve), and $\delta = 1.3^\circ > \delta_0$ (green dot-dashed curve) of the two beam components. For comparison, the black-solid curve shows the yield for a single driving beam, which is equivalent to $\delta = 0^\circ$. The spectra were obtained by using the RB-SFA package [55] that is based on a local forward ellipticity of the (purely time-dependent) vector potential. Since the even harmonic orders q are strongly suppressed, here we only display the yields for odd harmonics. Lines are just drawn to guide the eye. In (b), the intensity $I = 10^{14}$ W/cm^2, the wavelength $\lambda = 800$ nm, and an argon target ($I_p = 15.76$ eV) was assumed.

$\mathbf{d}(\mathbf{p}) = \langle \chi_{\mathbf{p}}(t)|\, \mathbf{r}\, |\Phi_0(t)\rangle$. To obtain the harmonics for two non-collinear beams, this matrix element as well as the associated time integrals have to be evaluated again with the nondipole Volkov states (9). In practice, this evaluation and analysis is quite demanding because of the explicit $\mathbf{r}$ dependence of the modified Volkov phase as well as the second order of the time and momentum integrations. In addition, the harmonic dipole moment is typically explored in length gauge and needs to first be reexpressed within the velocity gauge, before the nondipole Volkov solutions (9) from above can be utilized explicitly. This decomposition and (analytical) simplification of the harmonic dipole moments (21) is currently under work.

Figure 6(a) shows the harmonic yield in intense mid-IR laser fields, which is strongly suppressed for a single laser beam because of the Lorentz force [56]. To illustrate the rapid decrease of the harmonic yield, Fig. 6(a) displays the envelope of the harmonic spectrum for beams of three different wavelengths but the same intensity. For the sake of simplicity, these HHG spectra were computed for He^+ target ions and a single beam with intensity $I = 10^{15}$ W/cm^2. Figure 6(b), in contrast, shows the estimated yield of the odd harmonics, by applying different opening angles δ and for the near-IR wavelength $\lambda = 800$ nm as well as an argon target ($I_p = 15.76$ eV). While the black-solid curve exhibits the yield for a single driving beam ($\delta = 0^\circ$), the expected yields are also displayed for two not quite collinear beams with opening angles $\delta < \delta_o$ (red-dashed curve), $\delta \approx \delta_o$ (blue-dotted curve), and $\delta > \delta_o$ (green dot-dashed curve), respectively. These spectra were generated using the RB-SFA package [55] that is based on a local forward ellipticity of the (purely time-dependent) vector potential; cf. Refs. [46,57]. Since the even harmonics are all strongly suppressed for linearly polarized beams, we only display the yields of the odd harmonics and lines to just guide the eyes.

IV. CONCLUSIONS

As commonly known, both the electric *and* magnetic fields may play a significant role in the interaction of light (beams) and matter. While the electric-dipole field alone is often sufficient in order to explain the excitation or ionization of atoms qualitatively, care has to be taken with most *quantitative* predictions, and especially if the electrons probe rather large regions of the laser fields. The recent advances in strong-field ionization and HHG with mid-IR beams confirm this common knowledge and now call for theoretical methods and tools that help to go beyond the dipole approximation [58].

The motion of electrons in intense mid-IR fields makes the ionization of atoms sensitive especially to the magnetic or Lorentz forces. In this work, we have discussed in good detail how the nondipole Volkov solutions, originally developed in Ref. [26], enable us to analyze and understand phenomena such as the peak shifts in the momentum distribution of ATI photoelectrons or the compensation of the Lorentz force, if the ionization and generation of high harmonics is driven by crossed laser beams. Such a superposition of two beams also allows for exploring the Kapitza-Dirac deflection pattern of electrons that arise from atoms in intense standing waves, and which have found recurrent interest and application in matter optics [59].

In addition to the direct amplitude, it will be highly desirable to also apply the nondipole Volkov states (3) and (4) to the rescattering amplitude and to scrutinize in further detail Lorentz-force contributions for linearly polarized laser beams. Moreover, the explicit evaluation of the harmonic

dipole (or recombination amplitude) with these solutions will enable us to analyze more complex beam geometries in HHG and to consider novel schemes for table-top radiation sources.

ACKNOWLEDGMENT

This work has been funded by the Deutsche Forschungsgemeinschaft (DFG, German Research Foundation), Grant No. 440556973.

APPENDIX: NONDIPOLE VOLKOV STATES

1. Modified Volkov phase for general light fields with vector potential A(r, t)

The vector potential of any spatially structured light field can be generally expressed in terms of plane waves,

$$\mathbf{A}(\mathbf{r},t) = \int d^3\boldsymbol{k}\boldsymbol{A}(\boldsymbol{k},t) = \int d^3\boldsymbol{k}\mathrm{Re}\{\boldsymbol{a}(\boldsymbol{k})e^{i\,u_{\mathbf{k}}}\},$$
$$u_{\mathbf{k}} = \mathbf{k}\cdot\mathbf{r} - \omega\,t.$$

For such a (laser) field, the nondipole Volkov solution of an outgoing photoelectron is given by [26]

$$\chi_{\mathbf{p}}(\mathbf{r},t) = \frac{1}{(2\pi)^{3/2}} e^{i\,(\mathbf{p}\cdot\mathbf{r} - \frac{p^2}{2}\,t)} e^{-i\,\Gamma(\mathbf{r},t)},$$

with the modified Volkov phase [cf. Eq. (4)],

$$\Gamma(\boldsymbol{r},t) = \Gamma_1(\boldsymbol{r},t) + \Gamma_2(\boldsymbol{r},t) + \Gamma_3(\boldsymbol{r},t) + \mathcal{O}\left(\frac{\beta_0^{3/2}}{a_0\lambda^{1/2}}\right),$$

$$\Gamma_1(\mathbf{r},t) = \int d^3\boldsymbol{k}\rho_{\boldsymbol{k}}\sin\,(u_{\boldsymbol{k}} + \theta_{\boldsymbol{k}}),$$

$$\Gamma_2(\mathbf{r},t) = \int d^3\boldsymbol{k}\int d^3\boldsymbol{k}'[\alpha^+_{\boldsymbol{k}\boldsymbol{k}'}\,\sin(\theta^+_{\boldsymbol{k}\boldsymbol{k}'} + u_{\boldsymbol{k}} + u_{\boldsymbol{k}'}) + \alpha^-_{\boldsymbol{k}\boldsymbol{k}'}\sin(\theta^-_{\boldsymbol{k}\boldsymbol{k}'} + u_{\boldsymbol{k}} - u_{\boldsymbol{k}'})],$$

$$\Gamma_3(\mathbf{r},t) = \frac{1}{2}\int d^3\boldsymbol{k}\int d^3\boldsymbol{k}'\sigma_{\boldsymbol{k}\boldsymbol{k}'}\rho_{\boldsymbol{k}} \times\left(\frac{\sin\,(u_{\boldsymbol{k}} + u_{\boldsymbol{k}'} + \theta_{\boldsymbol{k}} + \xi_{\boldsymbol{k}\boldsymbol{k}'})}{\eta_{\boldsymbol{k}} + \eta_{\boldsymbol{k}'}} + \frac{\sin\,(u_{\boldsymbol{k}} - u_{\boldsymbol{k}'} + \theta_{\boldsymbol{k}} - \xi_{\boldsymbol{k}\boldsymbol{k}'})}{\eta_{\boldsymbol{k}} - \eta_{\boldsymbol{k}'}}\right).$$

For a (fixed) kinetic momentum $\mathbf{p}$ of the photoelectron, the individual functions $\lambda_{\mathbf{k}}$, $\theta_{\mathbf{k}}$, $\rho_{\mathbf{k}}$, $\alpha^{\pm}_{\boldsymbol{k}\boldsymbol{k}'}$, $\theta^-_{\boldsymbol{k}\boldsymbol{k}'}$, $\xi_{\boldsymbol{k}\boldsymbol{k}'}$, $\sigma_{\boldsymbol{k}\boldsymbol{k}'}$ in the Volkov phase can be obtained most easily by evaluating the left-hand sides of the following expressions with given plane-wave amplitudes $\mathbf{A}(\mathbf{k},t)$ and $\mathbf{a}(\mathbf{k})$ from above [26]:

$$\boldsymbol{p}\cdot\boldsymbol{A}(\boldsymbol{k},t) = \lambda_{\boldsymbol{k}}\cos\,(u_{\boldsymbol{k}} + \theta_{\boldsymbol{k}}), \qquad -\boldsymbol{k}\cdot\boldsymbol{A}(\boldsymbol{k}',t) = \sigma_{\boldsymbol{k}\boldsymbol{k}'}\cos(u_{\boldsymbol{k}'} + \xi_{\boldsymbol{k}\boldsymbol{k}'}),$$

$$\frac{1}{4}\boldsymbol{a}(\boldsymbol{k})\cdot\boldsymbol{a}(\boldsymbol{k}') = \Delta^+_{\boldsymbol{k}\boldsymbol{k}'}\exp(i\,\theta^+_{\boldsymbol{k}\boldsymbol{k}'}), \qquad \frac{1}{4}\boldsymbol{a}(\boldsymbol{k})\cdot\boldsymbol{a}^*(\boldsymbol{k}') = \Delta^-_{\boldsymbol{k}\boldsymbol{k}'}\exp(i\,\theta^-_{\boldsymbol{k}\boldsymbol{k}'}),$$

$$\rho_{\boldsymbol{k}} = \frac{\lambda_{\boldsymbol{k}}}{\eta_{\boldsymbol{k}}}, \qquad \alpha^{\pm}_{\boldsymbol{k}\boldsymbol{k}'} = \frac{\Delta^{\pm}_{\boldsymbol{k}\boldsymbol{k}'}}{\eta_{\boldsymbol{k}} \pm \eta_{\boldsymbol{k}'}}.$$

As seen from these equations, moreover, here $\rho_{\boldsymbol{k}}$ refers to the product of the kinetic and field-induced photoelectron momenta $[\boldsymbol{p}\cdot\boldsymbol{A}(\boldsymbol{k},t)]$ for a given Fourier mode $\boldsymbol{A}(\boldsymbol{k},t)$. Furthermore, the functions $\alpha^{\pm}_{\boldsymbol{k}\boldsymbol{k}'}$ denote the ponderomotive terms for each mode, $[\boldsymbol{a}(\boldsymbol{k})\cdot\boldsymbol{a}(\boldsymbol{k}')]$.

2. Modified Volkov states for two not quite collinear beams

For the vector potential (7)–(9) of two not quite collinear beams, the modified Volkov phase from Sec. 1 of this Appendix becomes

$$\Gamma(\boldsymbol{r},t) = \sum_{j=1}^{2}\left[\rho_{\epsilon,j}\sin\left(u_{\boldsymbol{k}_j} + \varphi^{(\epsilon)}_{p,j}\right) + \alpha^+_j\sin(2u_{\boldsymbol{k}_j}) - \alpha^-_j u_{\boldsymbol{k}_j}\right] + 2\,\alpha^+_{12}\,\sin\,(u_{\boldsymbol{k}_1} + u_{\boldsymbol{k}_2}) + 2\,\alpha^-_{12}\sin\,(u_{\boldsymbol{k}_1} - u_{\boldsymbol{k}_2}),$$

with

$$\rho_{\epsilon,j} = -\frac{A^{(0)}_j}{\omega_j\sqrt{1+\epsilon_j^2}}\frac{p^{(\epsilon)}_j}{1 - \boldsymbol{p}\cdot\boldsymbol{k}_j/\omega_j}, \quad u_{\boldsymbol{k}_j} = \mathbf{k}_j\cdot\mathbf{r}_j - \omega_j\,t, \quad j = 1,2,$$

$$\varphi^{(\epsilon)}_{p,1} = \arctan\left(\epsilon_1\frac{p_y}{p_x}\right), \quad \varphi^{(\epsilon)}_{p,2} = \arctan\left(\epsilon_2\frac{p_y}{p_x\cos\beta - p_z\sin\beta}\right),$$

$$\alpha^+_j = \frac{1}{2}\frac{\tilde{U}_{p,j}}{\omega_1}\frac{\epsilon_1^2 - 1}{\epsilon_1^2 + 1}, \quad \alpha^-_j = \frac{\tilde{U}_{p,j}}{\omega_j},$$

$$\alpha_{12}^{-} = \frac{A_1^{(0)} A_2^{(0)}}{4} \frac{1}{\sqrt{\left(1+\epsilon_1^2\right)\left(1+\epsilon_2^2\right)}} \frac{\cos\beta + \epsilon_1\epsilon_2}{\frac{p_z}{c}(\omega_1 - \omega_2\cos\beta) - \frac{p_x}{c}\omega_2\sin\beta - (\omega_1 - \omega_2)},$$

$$\alpha_{12}^{+} = \frac{A_1^{(0)} A_2^{(0)}}{4} \frac{1}{\sqrt{\left(1+\epsilon_1^2\right)\left(1+\epsilon_2^2\right)}} \frac{|\cos\beta - \epsilon_1\epsilon_2|}{\frac{p_z}{c}(\omega_1 + \omega_2\cos\beta) + \frac{p_x}{c}\omega_2\sin\beta - (\omega_1 + \omega_2)}.$$

As for a single beam in Sec. II B, $\rho_{\epsilon,1}$ and $\rho_{\epsilon,2}$ represent the products of the kinetic photoelectron momentum $\mathbf{p}_{1,2}$ with the momenta induced by the individual beams $\boldsymbol{A}_{1,2}$, while $\alpha_{1,2}^{\pm}$ capture the contributions of the modified ponderomotive energies $\tilde{U}_{p,j} = \frac{U_{p,j}}{1-\boldsymbol{p}\cdot\boldsymbol{k}_j/\omega_j}$, $j = 1, 2$, of the photoelectron. Similarly, the $p_j^{(\epsilon)}$ and $\varphi_{p,j}^{(\epsilon)}$ can be interpreted as the modulus and the azimuthal angle of the momentum vectors in Cartesian coordinates $\boldsymbol{p}_1^{(\epsilon_1)} = (p_x,\ \epsilon_1\, p_y,\ 0)$ and $\boldsymbol{p}_2^{(\epsilon_2)} = (p_x\ \sin\beta - p_z \sin\beta,\ \epsilon_2\, p_y,\ 0)$, respectively.

[1] P. Agostini, F. Fabre, G. Mainfray, G. Petite, and N. K. Rahman, Free-Free Transitions Following Six-Photon Ionization of Xenon Atoms, Phys. Rev. Lett. **42**, 1127 (1979).

[2] A. McPherson, G. Gibson, H. Jara, U. Johann, T. S. Luk, I. A. McIntyre, K. Boyer, and C. K. Rhodes, Studies of multiphoton production of vacuum-ultraviolet radiation in the rare gase, J. Opt. Soc. Am. B **4**, 595 (1987).

[3] F. Krausz and M. Ivanov, Attosecond physics, Rev. Mod. Phys. **81**, 163 (2009).

[4] G. J. Stein, P. D. Keathley, P. Krogen, H. Liang, J. P. Siqueira, C. L. Chang, C. J. Lai *et al.*, Water-window soft x-ray high-harmonic generation up to the nitrogen K-edge driven by a kHz, 2.1 μm OPCPA source, J. Phys. B: At. Mol. Opt. Phys. **49**, 155601 (2016).

[5] L. He, P. Lan, A. T. Le, B. Wang, B. Wang, X. Zhu, P. Lu, and C. D. Lin, Real-Time Observation of Molecular Spinning with Angular High-Harmonic Spectroscopy, Phys. Rev. Lett. **121**, 163201 (2018).

[6] J. Li, J. Lu, A. Chew, S. Han, J. Li, Y. Wu, H. Wang, S. Ghimire, and Z. Chang, Attosecond science based on high harmonic generation from gases and solids, Nat. Commun. **11**, 2748 (2020).

[7] P. B. Corkum and F. Krausz, Attosecond science, Nat. Phys. **3**, 381 (2007).

[8] T. Popmintchev, M.-C. Chen, D. Popmintchev, P. Arpin, S. Brown, S. Alisauskas, G. Andriukaitis, T. Balciunas, O. D. Mucke, A. Pugzlys *et al.*, Bright coherent ultrahigh harmonics in the keV X-ray regime from mid-infrared femtosecond lasers, Science **336**, 1287 (2012).

[9] M. C. Chen, P. Arpin, T. Popmintchev, M. Gerrity, B. Zhang, M. Seaberg, D. Popmintchev, M. M. Murnane, and H. C. Kapteyn, Bright, Coherent, Ultrafast Soft X-Ray Harmonics Spanning the Water Window from a Tabletop Light Source, Phys. Rev. Lett. **105**, 173901 (2010).

[10] C. Hernández-García, J. A. Perez-Hernandez, T. Popmintchev, M. M. Murnane, H. C. Kapteyn, A. Jaron-Becker, A. Becker, and L. Plaja, Zeptosecond High Harmonic keV X-Ray Waveforms Driven by Midinfrared Laser Pulses, Phys. Rev. Lett. **111**, 033002 (2013).

[11] J. Dura, N. Camus, A. Thai, A. Britz, M. Hemmer, M. Baudisch, A. Senftleben, C. D. Schröter, J. Ullrich, R. Moshammer, and J. Biegert, Ionization with low-frequency fields in the tunneling regime, Sci. Rep. **3**, 2675 (2013).

[12] M. Klaiber, K. Z. Hatsagortsyan, J. Wu, S. S. Luo, P. Grugan, and B. C. Walker, Limits of Strong Field Rescattering in the Relativistic Regime, Phys. Rev. Lett. **118**, 093001 (2017).

[13] B. Böning and S. Fritzsche, Partial-wave representation of the strong-field approximation, Phys. Rev. A **102**, 053108 (2020).

[14] B. Böning, P. Abele, W. Paufler, and S. Fritzsche, Above-threshold ionization of Ba^+ with realistic initial states in the strong-field approximation, J. Phys. B: At. Mol. Opt. Phys. **54**, 025602 (2021).

[15] T. Keil and D. Bauer, Coulomb-corrected strong-field quantum trajectories beyond dipole approximation, J. Phys. B: At. Mol. Opt. Phys. **50**, 194002 (2017).

[16] S. Chelkowski, A. D. Bandrauk, and P. B. Corkum, Photon-momentum transfer in multiphoton ionization and in time-resolved holography with photoelectrons, Phys. Rev. A **92**, 051401(R) (2015).

[17] H. C. Ni, S. Brennecke, X. Gao, P.-L. He, S. Donsa, I. Brezinova, F. He, J. Wu, M. Lein, X.-M. Tong, and J. Burgdörfer, Theory of Subcycle Linear Momentum Transfer in Strong-Field Tunneling Ionization, Phys. Rev. Lett. **125**, 073202 (2020).

[18] H. R. Reiss, Limits on Tunneling Theories of Strong-Field Ionization, Phys. Rev. Lett. **101**, 043002 (2008).

[19] A. Ludwig, J. Maurer, B. W. Mayer, C. R. Phillips, L. Gallmann, and U. Keller, Breakdown of the Dipole Approximation in Strong-Field Ionization, Phys. Rev. Lett. **113**, 243001 (2014).

[20] J. Maurer, B. Willenberg, J. Danek, B. W. Mayer, C. R. Phillips, L. Gallmann, M. Klaiber, K. Z. Hatsagortsyan, C. H. Keitel, and U. Keller, Probing the ionization wave packet and recollision dynamics with an elliptically polarized strong laser field in the nondipole regime, Phys. Rev. A **97**, 013404 (2018).

[21] B. Wolter, M. G. Pullen, M. Baudisch, M. Sclafani, M. Hemmer, A. Senftleben, C. D. Schroter, J. Ullrich, R. Moshammer, and J. Biegert, Strong-Field Physics with Mid-IR Fields, Phys. Rev. X **5**, 021034 (2015).

[22] L. V. Keldysh, Ionization in the field of a strong electromagnetic wave, Sov. Phys. JETP **20**, 1307 (1964).

[23] A. S. Titi and G. W. F. Drake, Quantum theory of longitudinal momentum transfer in above-threshold ionization, Phys. Rev. A **85**, 041404(R) (2012).

[24] K. Krajewska and J. Z. Kaminski, Radiation pressure in strong-field-approximation theory: Retardation and recoil corrections, Phys. Rev. A **92**, 043419 (2015).

[25] P.-L. He, D. Lao, and F. He, Strong Field Theories beyond Dipole Approximations in Nonrelativistic Regimes, Phys. Rev. Lett. **118**, 163203 (2017).

[26] B. Böning, W. Paufler, and S. Fritzsche, Nondipole strong-field approximation for spatially structured laser fields, Phys. Rev. A **99**, 053404 (2019).

[27] D. M. Wolkow, Über eine Klasse von Lösungen der Diracschen Gleichung, Z. Phys. **94**, 250 (1935).

[28] D B Milošević, G. G. Paulus, D. Bauer, and W. Becker, Above-threshold ionization by few-cycle pulses, J. Phys. B: At. Mol. Opt. Phys. **39**, R203 (2006).

[29] B. Böning, W. Paufler, and S. Fritzsche, Attosecond streaking with twisted X waves and intense infrared pulses, Phys. Rev. A **96**, 043423 (2017).

[30] B. Böning, W. Paufler, and S. Fritzsche, Above threshold ionization by few-cycle bessel pulses carrying orbital angular momentum, Phys. Rev. A **98**, 023407 (2018).

[31] L. Rosenberg, and F. Zhou, Generalized Volkov wave functions: Application to laser-assisted scattering, Phys. Rev. A **47**, 2146 (1993).

[32] B. Baghdasaryan, B. Böning, W. Paufler, and S. Fritzsche, Dichroism in two-color above-threshold ionization with twisted XUV beams and intense infrared laser fields, Phys. Rev. A **99**, 023403 (2019).

[33] B. Böning, W. Paufler, and S. Fritzsche, Polarization-dependent high-intensity Kapitza-Dirac effect in strong laser fields, Phys. Rev. A **101**, 031401(R) (2020).

[34] F. H. M. Faisal, Multiple absorption of laser photons by atoms, J. Phys. B: At. Mol. Phys. **6**, L89 (1973).

[35] H. R. Reiss, Effect of an Intense Electromagnetic field on a weakly bound system, Phys. Rev. A **22**, 1786 (1980).

[36] M. Y. Ivanov, M. Spanner, and O. Smirnova, Anatomy of Strong Field Ionization, J. Mod. Opt. **52**, 165 (2005).

[37] K. Amini, J. Biegert, F. Calegari, A. Chacon, M. F. Ciappina, A. Dauphin, D. K. Efimov, C. F. de Morisson Faria, and K. Giergiel, Symphony on strong field approximation, Rep. Prog. Phys. **82**, 116001 (2019).

[38] C. I. Blaga, F. Catoire, P. Colosimo, G. G. Paulus, H. G. Muller, P. Agostini, and L. F. DiMauro, Strong-field photoionization revisited, Nat. Phys. **5**, 335 (2009).

[39] S. V. Popruzhenko, Coulomb phase in high harmonic generation, J. Phys. B: At. Mol. Opt. Phys. **51**, 144006 (2018).

[40] W. Paufler, B. Böning, and S. Fritzsche, High harmonic generation with Laguerre-Gaussian beams, J. Opt. **21**, 094001 (2019).

[41] D. Bauer, D. B. Milosevic, and W. Becker, Strong-field approximation for intense-laser–atom processes: The choice of gauge, Phys. Rev. A **72**, 023415 (2005).

[42] S. Fritzsche, The RATIP program for relativistic calculations of atomic transition, ionization and recombination properties, Comput. Phys. Commun. **183**, 1525 (2012).

[43] C. T. L. Smeenk, L. Arissian, B. Zhou, A. Mysyrowicz, D. M. Villeneuve, A. Staudte, and P. B. Corkum, Partitioning of the Linear Photon Momentum in Multiphoton Ionization, Phys. Rev. Lett. **106**, 193002 (2011).

[44] A. Hartung, S. Eckart, S. Brennecke, J. Rist, D. Trabert, K. Fehre, M. Richter, H. Sann, S. Zeller, K. Henrichs *et al.*, Magnetic fields alter strong-field ionization, Nat. Phys. **15**, 1222 (2019).

[45] B. Böning and S. Fritzsche, Above-threshold ionization driven by Gaussian laser beams: Beyond the electric dipole approximation, J. Phys. B: At. Mol. Opt. Phys. **54**, 144002 (2021).

[46] E. Pisanty, D. D. Hickstein, B. R. Galloway, C. G. Durfee, H. C. Kapteyn, M. M. Murnane, and M. Ivanov, High harmonic interferometry of the Lorentz force in strong mid-infrared laser fields, New J. Phys. **20**, 053036 (2018).

[47] P. L. Kapitza and P. A. M. Dirac, The reflection of electrons from standing light waves, Math. Proc. Cambridge Philos. Soc. **29**, 297 (1933).

[48] L. Rosenberg, Effect of virtual compton scattering on electron propagation in a laser field, Phys. Rev. A **49**, 1122 (1994).

[49] H. Batelaan, Colloquium: Illuminating the Kapitza-Dirac effect with electron matter optics, Rev. Mod. Phys. **79**, 929 (2007).

[50] D. L. Freimund, K. Aflatooni, and H. Batelaan, Observation of the Kapitza-Dirac effect, Nature (London) **413**, 142 (2001).

[51] D. L. Freimund and H. Batelaan, Bragg Scattering of Free Electrons Using the Kapitza-Dirac Effect, Phys. Rev. Lett. **89**, 283602 (2002).

[52] P. H. Bucksbaum, D. W. Schumacher, and M. Bashkansky, High-Intensity Kapitza-Dirac Effect, Phys. Rev. Lett. **61**, 1182 (1988).

[53] W. Paufler, B. Böning, and S. Fritzsche, Tailored orbital angular momentum by high-harmonic generation from counterrotating Bi-circular Laguerre-Gaussian beams, Phys. Rev. A **98**, 011401(R) (2018).

[54] W. Paufler, B. Böning, and S. Fritzsche, Coherence control in high-order harmonic generation with Laguerre-Gaussian beams, Phys. Rev. A **100**, 013422 (2019).

[55] E. Pisanty, Rb-SFa: High Harmonic Generation in the Strong-Field Approximation via *Mathematica*, https://github.com/episanty/RB-SFA, doi:10.5281/zenodo.592519 (2020) (unpublished).

[56] M. W. Walser, C. H. Keitel, A. Scrinzi, and T. Brabec, High Harmonic Generation Beyond the Electric Dipole Approximation, Phys. Rev. Lett. **85**, 5082 (2000).

[57] A. Weber, B. Böning, B. Minneker, and S. Fritzsche, Generation of elliptically polarized high-order harmonic radiation with bi-elliptical two-color laser beams, Phys. Rev. A **104**, 063118 (2021).

[58] S. Fritzsche, A fresh computational approach to atomic structures, processes and cascades, Comput. Phys. Commun. **240**, 1 (2019).

[59] M. Arndt, A. Ekers, W. von Klitzing, and H. Ulbricht, Focus on modern frontiers of matter wave optics and interferometry, New J. Phys. **14**, 125006 (2012).